

ABSTRACT

Title of thesis: **Applications of Dynamic Light Scattering in
Chemical and Biomolecular Engineering:
Polymers, Proteins and Liquid Crystals**

Kirtland L. Linegar, Master of Science, 2008

Thesis directed by: Professor Mikhail A. Anisimov
 Institute for Physical Science and Technology and
 Department of Chemical and Biomolecular Engineering

Dynamic Light Scattering (DLS) is a powerful tool for probing soft-matter. The history, equipment, and basic theory of DLS is outlined. Three applications of DLS representing contemporary problems in chemical and biomolecular engineering are presented: polymers, proteins, and liquid crystals. DLS was performed on the polymer poly(ethylene glycol) in aqueous solutions to discern a conformational change from a coil to a helix when dissolved in isobutyric acid and to compare DLS and small angle neutron scattering (SANS) measurements. DLS experiments were conducted on the protein GroEL to determine the aggregation kinetics of the protein in solution. Finally, we observed a phenomenon never before seen associated with the relaxation of fluctuations of anisotropy and concentration fluctuations in a lyotropic chromonic liquid crystal solution of cromolyn. This phenomenon causes a significant increase of the effective relaxation time of the anisotropy fluctuations with an increase of the wave-number of the fluctuations.

Applications of Dynamic Light Scattering in Chemical Engineering:
Polymers, Proteins, and Liquid Crystals

by

Kirtland L. Linegar

Thesis submitted to the Faculty of the Graduate School of the
University of Maryland, College Park in partial fulfillment
of the requirements for the degree of
Master of Science
2008

Advisory Committee:

Professor Mikhail A. Anisimov, Chair/Advisor

Professor Jan V. Sengers

Professor Srinivasa Raghavan

Professor Sandra C. Greer

ACKNOWLEDGMENTS

I would like to thank my advisor, Professor Mikhail A. Anisimov for his trust, support, and mentorship. I also would like to thank Dr. Andrei Kostko from the Commonwealth University of Virginia who instructed me on the use of DLS equipment and aided in the data analysis. I thank all the members of our research group who have worked together in support of our combined research. Particularly, I want to acknowledge Chris Bertrand who has expended extraordinary efforts in providing a theoretical description of our results from the cromlyn research.

I wish to thank Professor Sandra Greer and her group for their partnership in the study of the conformation change in PEG. I also wish to thank Professor George Lorimer and Sarah Weheri for their partnership in our study of the GroEL protein aggregation.

I wish to thank the staff of the Department of Chemical and Biomolecular Engineering and of the Institute for Physical Science and Technology for their kind assistance.

I also want to thank my wife, Kacie, as well as my parents, for their love and support.

Finally, I wish to acknowledge the United States Coast Guard which has provided financial support for my graduate study.

TABLE OF CONTENTS

LIST OF FIGURES	viii
NOTATION	ix
CHAPTER 1 BACKGROUND	1
1.1 Introduction	1
1.2 History	2
1.3 Theory	5
1.4 Sample Preparation and Instrumentation	11
CHAPTER 2 POLYMER CONFORMATIONS AND SIZE MEASUREMENTS BY DLS	24
2.1 Polymers in Aqueous Solutions	24
2.2 Study of of Poly(ethylene glycol) in Solutions	25
2.3 Dynamic Light Scattering in Poly(ethylene glycol) Solutions	28
CHAPTER 3 PROTEIN AGGREGATION KINETICS BY DLS	39
3.1 Protein Folding and Aggregation	39
3.2 Chaperonin Protein GroEL	43
3.3 Aggregations Processes of GroEl Studied by DLS	46
CHAPTER 4 DYNAMICS OF PRE-TRANSITIONAL FLUCTUATIONS IN A LYOTROPIC CHROMONIC LIQUID CRYSTAL	54
4.1 Fluctuations in Pure Fluids, Binary Mixtures, and Polymer Solutions	54
4.2 Pre-transitional fluctuations of Liquid Crystals	58
4.3 Dynamic Light Scattering Study of Cromlyn Liquid Crystal Solution	61
CHAPTER 5 CONCLUSIONS	86
CHAPTER 6 APPENDIX A: CONTOUR PLOTS FROM DEPOLARIZED SCATTERING	88
CHAPTER 7 APPENDIX B: CONTOUR PLOT FROM POLARIZED LIGHT SCATTERING	100

REFERENCES CITED.....108

LIST OF FIGURES

<u>Figure</u>	<u>Page</u>
1.1 Block diagram of custom setup made for University of Maryland by Photocor Instruments	13
1.2 Photograph of the Photocor Instruments basic setup	14
1.3 Photograph of the customized Photocor Instruments DLS setup made for University of Maryland.	15
1.4 The temperature controlled shell consists of two electrically heated layers to maintain accurate temperature control.	15
1.5 A simplified block diagram of correlator operation.	17
1.6 A screen shot of the Photocor-FC GUI.	18
1.7 A screen shot from DynaLS software.	19
1.8 Screen shot of ALV software	20
2.1 Coexistence curve of isobutyric acid and water according to Toumi <i>et al.</i> ¹⁶	26
2.2 Measurements of the refractive index of IBA-water binary solution for three volume fractions of water at different temperatures.	29
2.3 The shear viscosities of IBA, Water, and IBA-water binary solutions as a function of temperature. The plots for the pure liquids are made from the Arrhenius equation given in the CRC handbook. ²¹ The plotted lines for the binary liquids are Arrhenius fits to data from Ourfelli <i>et al.</i> ¹⁹ made using Matlab.	31
2.4 The measured correlation function for 20KOH PEG in water. The solid line is a single exponential fit to the correlation function computed by Matlab.	33
2.5 DynaLS computed probability distribution function for PEG in D2O. . .	34
2.6 DynaLS computed probability distribution function for PEG in H2O. . .	34
2.7 DynaLS computed probability distribution function for PEG in IBA. . .	35
2.8 Table of radius measurements for 20KOH PEG in solution by different methods.	36
3.1 Results from TMV study by Panyukov et al. ²⁵ Left: Intensity increases as a function of time until it reaches a critical level where the rate of precipitation is equal to the rate of formation of new aggregates. Right: The rate of gyration increases linearly at short time before splitting and forming two separate types of aggregates.	41
3.2 Results from TMV study by Panyukov <i>et al.</i> ²⁵ show the increase of the radius of gyration with time of aggregates when three different molarities of CTAB are added to the solution at 25°C	41
3.3 Computer generated image of GroEL viewed from side. ³⁶	44
3.4 Computer generated image of GroEL when viewed from an end. ³⁶	44
3.5 The correlation function measured from a sample of GroEL after two weeks at 22°C.	47
3.6 Correlation function for GroEL measured at 37°C.	48

3.7	A plot of the normalized intensity of scattered light versus time. The normalized intensity scale for the 20% acetone solution (circles) is on the left y-axis. The normalized intensity for the 10% acetone solution (diamonds) is on the right y-axis.	49
3.8	Normalized intensity plots for a 3.5 μM GroEL concentration sample (top) and 1.5 μM GroEL concentration sample (bottom) both in 20% acetone solution.	50
3.9	Four probability size distributions from DynaLS analysis of correlation functions taken at elapsed times for the 3.5 μM GroEL concentration sample with 20% acetone.	52
4.1	(a) A representation of the probability distribution analysis of the correlation function for the largest polymer sample observed with molecular weight $11.4 \times 10^{-6} \text{g} \cdot \text{mol}^{-1}$ measured at $\theta = 30^\circ$ in the form of a 3-D graph. (b) gives the same graph as a grey-scale plot. ⁴⁶	57
4.2	Structure diagram of Cromlyn ⁵⁴	62
4.3	Phase diagram for lyotropic chromonic liquid crystal Cromlyn. ⁵⁵	63
4.4	Example of a contour plot for the probability distribution of relaxation times versus temperature.	64
4.5	Inverse intensity of vertically polarized light scattering at scattering angle $\theta = 120^\circ$ as a function of temperature. Open circles represent experimental data. Dashed line shows the linear approximation, valid below 35°C . Dotted line represents the Landau-de Gennes behavior for the nematic susceptibility χ_o^{-1} given by equation (4.8) and magnified in the inset. The dotted line is shifted down from the dashed line by a constant proportional to $\xi_o^2 q^2$. The temperature $T^* \simeq 30^\circ\text{C}$ is the absolute limit of the isotropic phase, $T_A \simeq 45^\circ\text{C}$ indicates the onset of cromolyn aggregation.	67
4.6	An Ornstein-Zerike plot of the inverse intensity of the anisotropic scattering in the isotropic phase of cromolyn solution at 33.65°C as a function of the wave number obtained with the alternative setup and use of immersion.	69
4.7	Examples of the dynamic auto-correlation functions at $\theta = 15^\circ$ (a) and $\theta = 150^\circ$ (b) obtained with the ALV correlator (a) and the PhotoCor correlator (b). The PhotoCor correlator allows obtaining the correlation function at $t < 5 \cdot 10^{-3}$ ms.	72
4.8	Stretched exponential parameter as a function of temperature.	73
4.9	Decay times for the VH alignment of light scattering in the isotropic phase of cromolyn solution at $\theta = 15^\circ$ (a) and $\theta = 150^\circ$ (b). The contour maps show equal probability distributions of decay times. The open circles show maxima of the probability distributions. The crosses indicate average decay times obtained from the fits of the correlation functions to stretched exponentials given by Eq. (4.10).	74
4.10	Average ("effective") decay times of the anisotropic fluctuations in the isotropic phase of cromolyn solution as a function of temperature. The symbols indicate different scattering angles as in figure 4.8.	74

- 4.11 Top: Average decay rates of anisotropic fluctuations in the isotropic phase of cromolyn solution as a function of the light-scattering wave number for different selected temperatures. Symbols indicate various temperatures. Solid lines are q^2 -linear approximations as given by Eq. (4.12). The data for 32.7°C were collected only for two angles: $\theta = 19^\circ$ and $\theta = 105^\circ$. Bottom: Uncoupled decay rates of fluctuations of anisotropy, τ_0 , as a function of temperature. The open circles are the values obtained by extrapolation of $\tau_{\text{VH}}(q)$ to $q = 0$. The dashed curve is fit to Eq. (4.13). The coupling length is shown in inset as a function of temperature (crosses) with a solid line denoting the average. 75
- 4.12 The q -dependence of the anisotropic fluctuations is shown using two different DLS equipment setups. Data from the original instrument are represented by stars while data from a second instrument have been analyzed by two separate methods represented by circles and squares. 78
- 4.13 Decay times for the VV alignment of light scattering in the isotropic phase of cromolyn solution at $\theta = 15^\circ$ (a), $\theta = 30^\circ$ (b), $\theta = 45^\circ$ (c), and $\theta = 150^\circ$ (d) . The contour maps show equal probability distributions of decay times. The two almost parallel lines indicate two uncoupled diffusion modes as predicted by Eq. (4.16) from the data obtained at about 39°C. The solid curve represents the behavior of the effective relaxation time of the anisotropy fluctuations obtained from the VH light scattering alignment, as given by Eq. (4.12). . . . 79
- 4.14 Wave-number dependence of the inverse diffusion times of the isotropic fluctuations at selected temperatures: for slow diffusion (top) and for fast diffusion (bottom). Symbols show the experimental data, solid straight lines indicate the approximations given by Eq. (4.15). . . . 82
- 6.1 Contour plot for 15°scattering angle and VV alignment. Darker color contour areas represent higher probability for the relaxation time. . . 89
- 6.2 Contour plot for 19°scattering angle and VV alignment. Darker color contour areas represent higher probability for the relaxation time. . . 90
- 6.3 Contour plot for 30°scattering angle and VV alignment. Darker color contour areas represent higher probability for the relaxation time. . . 91
- 6.4 Contour plot for 45°scattering angle and VV alignment. Darker color contour areas represent higher probability for the relaxation time. . . 92
- 6.5 Contour plot for 60°scattering angle and VV alignment. Darker color contour areas represent higher probability for the relaxation time. . . 93
- 6.6 Contour plot for 75°scattering angle and VV alignment. Darker color contour areas represent higher probability for the relaxation time. . . 94
- 6.7 Contour plot for 90°scattering angle and VV alignment. Darker color contour areas represent higher probability for the relaxation time. . . 95
- 6.8 Contour plot for 109°scattering angle and VV alignment. Darker color contour areas represent higher probability for the relaxation time. . . 96
- 6.9 Contour plot for 120°scattering angle and VV alignment. Darker color contour areas represent higher probability for the relaxation time. . . 97

6.10	Contour plot for 135° scattering angle and VV alignment. Darker color contour areas represent higher probability for the relaxation time. . .	98
6.11	Contour plot for 150° scattering angle and VV alignment. Darker color contour areas represent higher probability for the relaxation time. . .	99
7.1	Contour plot for 15° scattering angle and VH alignment. Darker color contour areas represent higher probability for the relaxation time. . .	101
7.2	Contour plot for 30° scattering angle and VH alignment. Darker color contour areas represent higher probability for the relaxation time. . .	102
7.3	Contour plot for 45° scattering angle and VH alignment. Darker color contour areas represent higher probability for the relaxation time. . .	103
7.4	Contour plot for 75° scattering angle and VH alignment. Darker color contour areas represent higher probability for the relaxation time. . .	104
7.5	Contour plot for 120° scattering angle and VH alignment. Darker color contour areas represent higher probability for the relaxation time. . .	105
7.6	Contour plot for 135° scattering angle and VH alignment. Darker color contour areas represent higher probability for the relaxation time. . .	106
7.7	Contour plot for 150° scattering angle and VH alignment. Darker color contour areas represent higher probability for the relaxation time. . .	107

Notation

β , stretching parameter

C_p , isobaric heat capacity

C_v , isochoric heat capacity

c , speed of light

c_n , number of molecules per unit volume

D , diffusion coefficient

E , electric field

E_o , amplitude of the electric field

η , shear viscosity

ε , permittivity of free space

Γ , relaxation rate

Γ_o , uncoupled relaxation rate of anisotropy fluctuations

h , extinction coefficient

I , intensity of light scattering

k , wave vector of incident light

k_B , Boltzmann's constant

l , length (general)

l_o , characteristic length of anisotropic molecules

$\Lambda_{1,2}$, characteristic length of anisotropic fluctuations

λ , wavelength of light

λ_o , temperature independent length scale of anisotropic fluctuations

M_w , weight average molecular weight

M_n , number average molecular weight

N , degree of polymerization

N_A , Avagadro's number

n , refractive index

q , wave number of light scattering

R_g , radius of gyration

R_h , hydrodynamic radius

t , time

T^* , second-order phase transition temperature

T_A , aggregation temperature

T_{NI} , isotropic-nematic transition temperature

τ , relaxation time (Γ^{-1})

τ_c , correlation time (general)

τ_q , q -dependent relaxation time

τ_R , non-conserved relaxation time (non- q -dependent)

τ_{ve} , viscoelastic relaxation time of polymers

u , speed of sound

ξ , correlation length

ξ_0 , amplitude of the correlation length

χ , susceptibility

χ_0 , susceptibility in the thermodynamic limit ($q \rightarrow 0$)

ω , frequency

CHAPTER 1

BACKGROUND

1.1 Introduction

Light scattering has been a topic of human fascination since the beginning of history. Often the first question of a child is, "Why is the sky blue?". Only in the last two centuries has the human race succeeded to fully describe this phenomenon and determine why we see the colors we see. As is often the human way of going about things, we set out not only to describe phenomena, but to harness that knowledge and utilize it as a tool of further inquisition. Our understanding of light and electromagnetic radiation has enabled us to develop multiple forms of spectroscopy comprising the entire electromagnetic radiation spectrum. In this thesis I shall focus on the applications of one form of spectroscopy, namely, Photon Correlation Spectroscopy (PCS), more commonly known as Dynamic Light Scattering (DLS). In order to understand this tool, we must first understand the basic concepts of electromagnetic radiation including how molecules scatter light, how we can capture this light, and how we can count and correlate the light photons to determine properties of the molecules that scattered it. After we have an understanding of how DLS works, we can then see how such a useful tool can be applied to a wide range of chemical engineering topics from simple macromolecule size measurements to critical phenomena and even to monitoring aggregation kinetics.

1.2 History

The earliest work in light scattering was conducted by Lord Rayleigh from 1870 to the beginning of the 20th century.² As both a theoretician and an experimentalist, he was the first person to correctly explain the color of the sky. Past theories had suggested that dust particles caused inhomogeneities in the atmosphere that scattered light. Theoretical calculations were correct in showing that this was a very plausible theory, but then experimentally it was shown that the intensity of the blue light was greater at higher altitudes, such as mountain tops, where there was less dust.² The answer, as Rayleigh found, was that light can in fact be scattered from an apparently homogenous medium. What Rayleigh understood was that in a given system, in order for light to be scattered, there must be some change in the refractive index at the point from which light is scattered. If a person stands in a room, and light enters the room through a window, the person would observe the light as it illuminates an area below the window. More often than not, the person also observes a "beam" between the window and floor which consists of dust particles that have refractive indices different from that of the surrounding air and create a non-homogeneous system. This sort of scattering was well known to Rayleigh, and is known as Mie scattering, which occurs when the wavelength of the light is smaller than the size of the particle.¹ Rayleigh realized that scattering also takes place in a continuously homogeneous medium of small particles or molecules because the particles are continuously undergoing Brownian motion and randomly moving. As the particles move, they create fluctuations in the density of the medium, which in

turn, create fluctuations in the refractive index of the medium, and scatter light.

Rayleigh's initial work was greatly expounded upon by Debye (1915) and Gans (1925). All of these early observations were limited in theory to gases whose molecules were of a spherical shape and whose refractive index was near unity.¹ It was not until Einstein and Smoluchowski took up the subject in 1908 and 1910 that real progress was made, paving the way for the modern theory of light scattering to be formulated. It was Einstein and Smoluchowski who, investigating the phenomena of critical opalescence in liquids, quantified the thermal fluctuations within a system which result in the inhomogeneities of the refractive index necessary for scattering. They developed the fluctuation theory of light scattering.³ The theory states that the intensity of scattered light can be determined by the mean-square fluctuations in density and/or concentration, which in turn are known from macroscopic properties, namely, isothermal compressibility and the osmotic compressibility.¹ To simplify this we can imagine a body of water, say 1 liter in volume. We can measure the mass of this body and divide its mass by its volume and declare confidently that it has a density of 1 g/cm^3 . Now, say we have another sample of water, but this time it is only comprised of a hundred molecules of water and we wish to measure its density. Because of thermal fluctuations, or Brownian motion, we would suddenly find ourselves in a bit of a pickle. As we try to measure the volume of these molecules they continue to move about. Now we find that the density changes with every measurement. Luckily, we are smart: we make multiple measurements and average them all together. If we made enough measurements and controlled the environment properly, we should get the same answer as when we had a full liter of water. We

have now learned that on a mesoscopic scale, macroscopic properties such as density, pressure, concentration, and even temperature undergo fluctuations which in turn affect the continuity of the refractive index and cause light to scatter.

After the time of Einstein and Smoluchowski, work in the area of light scattering would slow greatly as great leaps and bounds were made in Quantum Mechanics, the "nanotechnology" of the day. Debye and Zimm would continue to work on problems in light scattering through the 1940's. Mainly they looked to expand upon the theories of Brillouin and Mandelstam who predicted the Brillouin-Mandelstam doublet (1914, 1922).⁴ The doublet, as Brillouin and Mandelstam predicted, is caused by phonons, which are quasi-particles of sound somewhat similar to photons. When light passes through a medium, it is scattered by phonons, creating two peaks flanking the Rayleigh (central) line in the frequency spectrum. The doublet was actually observed by Gross in the 1930's,⁵ and Landau and Placzek explained the nature of the doublet and Rayleigh Line in 1934.⁴ The discovery and explanation of the Brillouin-Mandelstam doublet led to Landau and Placzek's discovery of the Landau-Placzek ratio which would form the basis for all further development in the area of light scattering.¹ The ratio of the amplitudes of the Brillouin-Mandelstam peak and Rayleigh line was related to a ratio of heat capacities as shown in section 1.3.

After this period, light-scattering studies would almost completely cease until the invention of lasers in the 1960's. Light scattering's doldrums of scientific progress were broken by the significant contributions of Fabelinskii in Russia⁴ and Pecora in the United States.¹² The laser would greatly propel the field of light scattering forward and solidify its position in physics for the second half of the 20th

century. Pecora would make significant progress in showing that scattered light can be used to determine diffusion coefficients and molecular-weight measurements as just a few of many applications to be further discussed.² Fabelinskii had spent a significant amount of time prior to the invention of the laser studying light scattering in liquids, gases, and crystals.⁴ His work was accelerated greatly by the laser, but equally as important, advances in integrated circuit technology gave scientists, such as Yudin *et al.*,^{7, 8, 9, 10} an edge in obtaining the time-dependent correlation functions. The Fabry-Perot interferometer served to increase the definition achievable in the frequency domain, while the invention of high speed correlators would achieve great accuracy within the time domain.

1.3 Theory

In treating the theory of light scattering, it is most important to understand light as both a wave and particle. We will retrace the thoughts of Rayleigh as he studied Maxwell's theories of electromagnetic radiation and built his own ideas on scattering. First we note the wavelike properties of light which can be described by the electric field $E(r, t)$:¹

$$E(r, t) = E_0[k \cdot r - \omega t], \tag{1.1}$$

where the frequency ω is related to the wavelength λ by the speed of light, $c = \lambda\omega$, and E_0 is the amplitude of the wave, and $k = 2\pi/\lambda$ is the wave vector. For this equation r and t are space coordinate and time respectively. The wavelength of light

is often cited when determining what we perceive as the color of the light. Human eyes can visually perceive a small range of EM radiation, a small portion of the spectrum squeezed between UV radiation and IR radiation.

The average intensity of light, measured in watt·cm⁻² is related to the electric field by:⁴

$$\langle I \rangle = \frac{cn |E|^2}{4\pi}, \quad (1.2)$$

where c is the speed of light, n is the refractive index, and E is the electric field of the scattered light wave. The refractive index is related to the permittivity of free space by $n \approx \sqrt{\epsilon}$. Lord Rayleigh's famous contribution to this theory was in relating the intensity, of the scattered light to its wavelength in a gas:^{2, 4}

$$I = I_o \frac{2\pi^2 V}{L^2 \lambda^4 N_A} (n - 1)^2 \sim \frac{1}{\lambda^4}, \quad (1.3)$$

where N_A is the Avogadro's Number, V the volume, and L the distance to the point of observation. The inverse relation of wavelength to the intensity is sometimes called the Rayleigh law and explains the blue color of the sky since blue light has a short wavelength.⁴ Furthermore it was shown that the extinction of light as it passed through a medium over a distance x was directly related to its intensity $I = I_0 e^{-hx}$ with $h = f(n, \lambda)$ being the extinction coefficient. The extinction coefficient varies widely depending on the medium and even in the atmosphere varies greatly depending on the content of dust and water in the air as well as the atmospheric pressure. However, in general, short wavelength visible light is dissipated at a much

greater rate than long wavelength light, and the sun appears reddish at sunset when the light must pass through the greatest amount of atmosphere before reaching the observer. Another result of this is that the variance of the extinction coefficient depending on atmospheric conditions has allowed for sailors to predict the weather based on the color of sunset and sunrise: a deeper red indicating a higher water content in the atmosphere or higher atmospheric pressure.

It must be noted that this intensity only accounts for light scattered from fluctuations of individual molecules. If two light emitting bodies are a distance $\ell = \lambda/(2 \sin \theta)$ apart, they will emit light in phase opposition which will cancel one another out (θ being the angle between the incident and scattered light).⁴ Only as bodies move in thermal motion will they pass in and out of phase opposition; and so, we must sum over an entire volume of particles to find the intensity of the scattered light.

The motion of light emitting particles is the diffusivity and is characterized by the particle diffusion coefficient. The diffusion coefficient D of non-interacting Brownian particles is given by the Einstein-Stokes equation:⁶

$$D = \frac{k_B T}{6\pi\eta R_h}, \tag{1.4}$$

where R_h is the hydrodynamic radius, η is the shear viscosity of the solvent, T is the absolute temperature, and k_B is the Boltzmann constant. From this it becomes understandable how one can obtain the hydrodynamic radius from measuring scattered light. To do this requires an understanding of stochastic processes and a small

invention; which nearly coincided with the invention of the laser: the integrated circuit. For a laser, the light from the incident beam has a single wavelength. Measuring the scattering signal as the incident beam passes through the sample, we can obtain the power spectrum by viewing the signal in the frequency domain. For simplicity we will use A to be the measured signal, and P as the power spectrum. The power spectrum in the frequency domain takes the form:¹

$$I_A(\omega) = \frac{1}{2\pi} \int dt e^{-i\omega t} \langle A^*(0)A(t) \rangle, \quad (1.5)$$

where A^* is the complex conjugate of A , and ω is the frequency. For the case of monodisperse Brownian particles this results in a Lorentzian with the form:²

$$I(\omega) = \frac{2Dq^2/\pi}{\omega^2 + (2Dq^2)^2}. \quad (1.6)$$

The wave number q is:

$$q = \frac{4\pi}{\lambda} \sin \frac{\theta}{2}, \quad (1.7)$$

where θ is the angle between the incident beam and the scattered light. Then the half-width of the Rayleigh line gives us the relaxation rate which is related to the diffusion coefficient:¹⁰

$$\Gamma = Dq^2. \quad (1.8)$$

The power spectrum of a monodisperse system will also be accompanied by

a Brillouin doublet which is frequency shifted from the peak by $\pm\Delta\omega$ where:

$$\Delta\omega \sim \frac{c}{u}, \quad (1.9)$$

which is the speed of light, c , over the speed of sound, u .¹² The ratio of the intensity of the central Rayleigh line to the intensity of the Brillouin doublet is the Landau-Placzek ratio:¹

$$\frac{I_R}{I_{Br}} = \frac{C_p - C_v}{C_v}, \quad (1.10)$$

where C_p is the isobaric heat capacity and C_v is the isochoric heat capacity. Taking the Fourier transform of the signal switches the frequency domain for the time domain. The Fourier transform of the power spectrum is the autocorrelation function.¹¹ Modern experiments can now directly measure the time-dependent intensity-correlation function using a correlator. For a signal A , the general form of the correlation function is:¹

$$\langle A(0)A(\tau) \rangle = \lim_{T \rightarrow \infty} \frac{1}{T} \int_0^T dt A(t)A(t + \tau). \quad (1.11)$$

In order to correlate two events, one at time t and one at time $t + \tau$, the time difference τ must be small in comparison with the event and the total measured interval T must be large compared to the event. For our purposes in light scattering the time difference must be significantly small compared to the fluctuations being observed. When this is true, and τ is small, then the value of the correlation function

will be at a maximum, of $\langle A^2 \rangle$. When the reverse is true, and τ is infinite compared to the time of fluctuation, then the correlation function takes on a minimum value of $\langle A \rangle^2$. In most cases that are applicable to light scattering the system will decay from the maximum to the minimum value as a single exponential of the form:¹

$$\langle A(0)A(\tau) \rangle = \langle A \rangle^2 + [\langle A^2 \rangle - \langle A \rangle^2] \exp\left(-\frac{\tau}{\tau_c}\right). \quad (1.12)$$

It is important to note here that the correlation time, τ_c , is not defined by the decaying exponential. In fact, because the correlation function may decay as multiple exponentials or as a non-exponential function, a more general definition of the correlation time is required:¹

$$\tau_c = \int_0^{\infty} d\tau \frac{\langle \delta A(0)\delta A(\tau) \rangle}{\langle \delta A^2 \rangle}. \quad (1.13)$$

It is also important to describe another aspect of the fluctuations when computing the correlation function. The correlation function measures a series of intensities over long period of time and determines the correlation between those times. The intensity is in turn dependent on the number of particles diffusing within the sample area, which is of course dependent on the volume of the sample area. Thus we define an area of coherence:²

$$A_{\text{coh}} = \pi b^2 = \frac{\lambda^2 l^2}{\pi a^2}. \quad (1.14)$$

The radius of the detector is b , l is the distance of the detector from the scattering

volume, and a is the radius of the scattering volume. It is important for signal quality that the radius of the detector be maintained so that the number of coherence areas measured be near unity. As we increase the number of coherence areas we detect above unity, we will lose definition in our signal. In order to maintain the coherence area it is necessary to ensure that the width of the source beam is larger than detector area.

1.4 Sample Preparation and Instrumentation

Sample Preparation: Sample preparation is one of the most important steps of any light-scattering experiment. As with any experiment, contaminants and sloppy handling practices can yield poor and inaccurate results. This is particularly the case for DLS due to the nature of the properties being measured. When conducting light-scattering experiments, the goal is to measure mesoscale fluctuations which are very sensitive to any perturbations. Any stray light, dust, or moisture can completely ruin an experiment. Thus the utmost care must be taken before, during, and after preparing a sample to ensure that no contamination of the sample takes place. Because most standard laboratory techniques are common knowledge and need not be re-iterated, I only discuss problems specific to light scattering.

The cell used to hold the sample is the first thing that must be considered when preparing a sample. In some cases the experiment may require high-quality optical glass for the sample cell. In most cases, though, standard clear glass cells free of any major defects will suffice. It is important that the size of the cell be chosen based on the amount of sample available. The light source must be able

to pass through the sample without any major disturbances in the refractive index. Thus there must be enough sample relative to the size of the container so that the laser beam is able to pass between the bottom of the cell and the lowest part of the vapor-liquid meniscus without being scattered at either interface. Also, each cell should be thoroughly rinsed and cleaned prior to use to remove dust or contaminants.

Secondly, choosing the type and size of filter will be one of the most important decisions in any sample preparation. It is important, particularly when working with acids or hydrocarbons, that the filter membrane is not soluble in the sample solvent. The filter pore size is also a necessary consideration when preparing the sample. If you already have *a priori* knowledge of the size of the particles to be measured, then you can choose the smallest pore size that will still allow the particles to pass. If not, then a larger pore size can be chosen until some initial measurements are made. When filtering, the first few drops of sample that pass through the filter should be discarded as waste. These first drops often contain dust and contaminants and are a rinse for the filter. One pass through the filter is often not enough. The sample should be filtered several times, keeping in mind that although the particles are smaller than the pore size, there will be some reduction in the particle concentration for each time the sample is filtered.

DLS Setup: The instruments used to conduct light scattering can vary greatly, and like all scientific instruments are tailored to their specific usage. A block diagram of the operation of light scattering equipment is given in figure 1.1. The devices

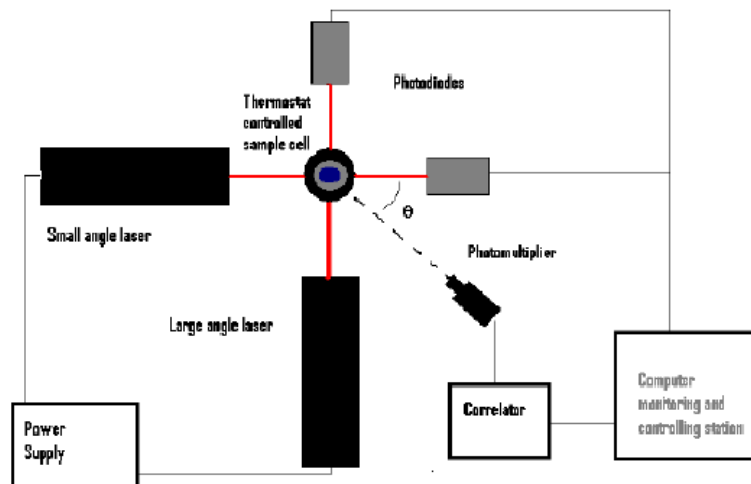


Figure 1.1: Block diagram of custom setup made for University of Maryland by Photocor Instruments

used in Dr. Anisimov's laboratory at the University of Maryland are designed for conducting experiments requiring precisely controlled temperatures at atmospheric pressure. Since long accumulation times are required by many studies, the equipment is designed to run automated experiments. The DLS setups available in this laboratory were manufactured by Photocor Instruments. Two different setups are currently in use. The first consists of a single laser and a photon counting unit mounted on a goniometer which is centered around a thermostat-controlled temperature shell. A photograph of this instrument setup is shown in figure 1.2. This basic setup is capable of temperature control within a tenth of a degree Kelvin. The second setup is a custom built apparatus made specifically for our laboratory at the University of Maryland. This setup, shown in figure 1.3, has an additional laser and two addition photodiodes that monitor the laser intensities. This setup is capable of digitally maintaining the temperature within a thousandth of a degree Kelvin. In

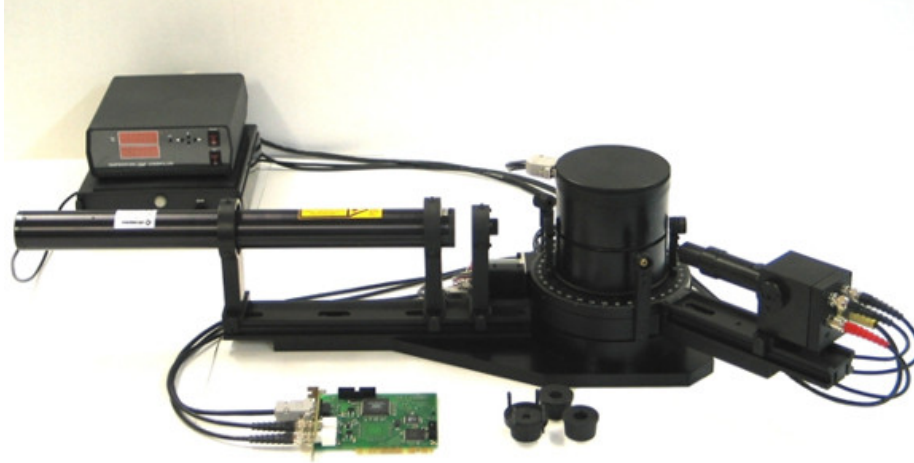


Figure 1.2: Photograph of the Photocor Instruments basic setup

both setups, the samples can be cooled using a temperature bath.

Both of these devices are now equipped with a special photon counting systems that contains dual photomultiplier tubes (PMT). This provides a unique advantage over single PMT counting systems in that the dual PMT systems allow for cross correlation computations that greatly increase both the accuracy and definition of the correlation function by eliminating after-pulses. As the correlation function measured over a time period T is given by:

$$G(\tau) = \frac{\lim_{T \rightarrow \infty}}{T} \int_0^T A(t)A(t + \tau)dt, \quad (1.15a)$$

the cross correlation function is then:

$$G(\tau) = \frac{\lim_{T \rightarrow \infty}}{T} \int_0^T A(t)B(t + \tau)dt, \quad (1.16)$$

where A and B are now two different signals.

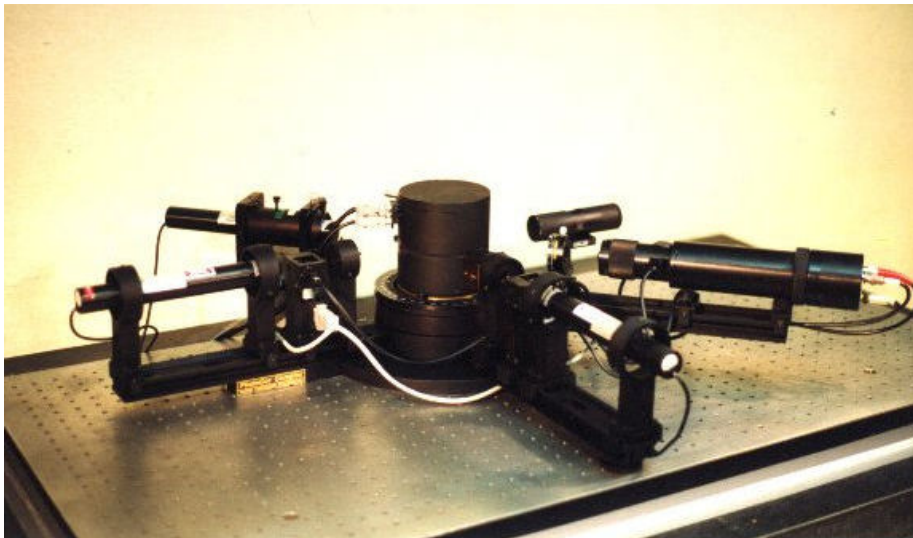


Figure 1.3: Photograph of the customized Photocor Instruments DLS setup made for University of Maryland.

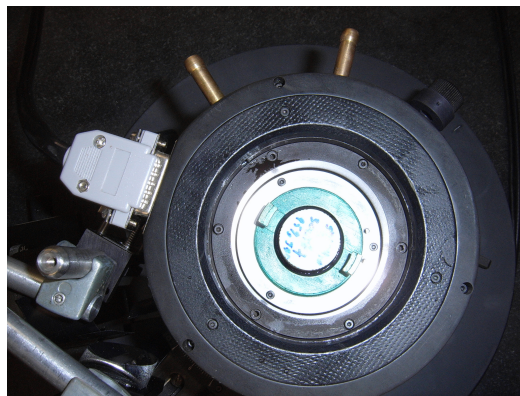


Figure 1.4: The temperature controlled shell consists of two electrically heated layers to maintain accurate temperature control.

The laser used with these devices is a 10 mW He-Ne laser with a wavelength of 633 nanometers. The laser is fed from a stabilized power supply to ensure that the laser output is consistent over the entire length of an experiment. The customized setup is also equipped with special automated shutters that are capable of blocking one or both of the lasers. These shutters enable measurement from two angles set 90 degrees apart from one another. The signal from the PMTs are then directed to the correlator device.

As the signal enters the correlator, the correlator will record the intensity, or number of counts, made at time t . The correlator then sends this information to a shift register counter and records a new intensity at time $t+\Delta\tau$. At this time the data from time t is then sent to the next shift register and the data from time t and $t+\Delta\tau$ are sent to the adders. The data are then added together with the previous information maintained in the correlation function memory. By adding previous information to current information, we are able to "correlate" what would otherwise appear to be a random set of data. A simplified diagram of correlator operation is given in figure 1.5.

Equally as important as the correlator hardware is the software used for computations from the correlation function. Three programs are used to collect and analyze correlation functions. Our primary software is the Photocor-FC software. This software is used to interact with the correlator board, thermostat, shutters, and exchange information with other software. Photocor provides great flexibility in data collection processes by enabling the user to write macro scripts that can be used to automate the measurement process. Photocor Instruments has continually

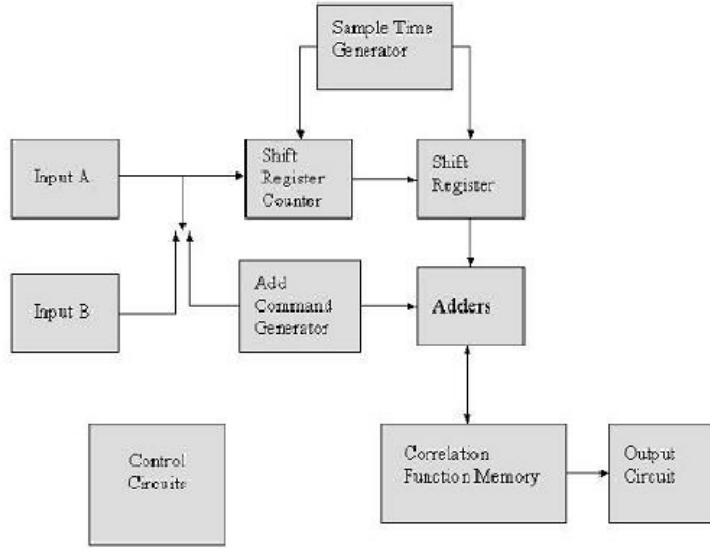


Figure 1.5: A simplified block diagram of correlator operation.

upgraded their software and recently has released Photocor v38 which is unique in its cutting edge dust cut-off software which enables the user to omit data points that have been spoiled by dust or other unwanted particles passing through the sample volume. The program works by splitting the accumulation of the correlation function into multiple tiny segments and then summing them together after omitting segments in which the intensity exceeds a pre-set maxima determined by the user (this is further discussed in Chapter 2).

Once the correlation function has been measured, Photocor exports the data to *DynaLS*. Alango DynaLS software uses the correlation functions and the physical parameters of a particular experiment and produces an analysis in the form of a probability distribution. The type of probability distribution, whether particle size or relaxation time, is set by the user. Size distributions are based on the assumption that the measured particles are spheres that move randomly in accordance with the

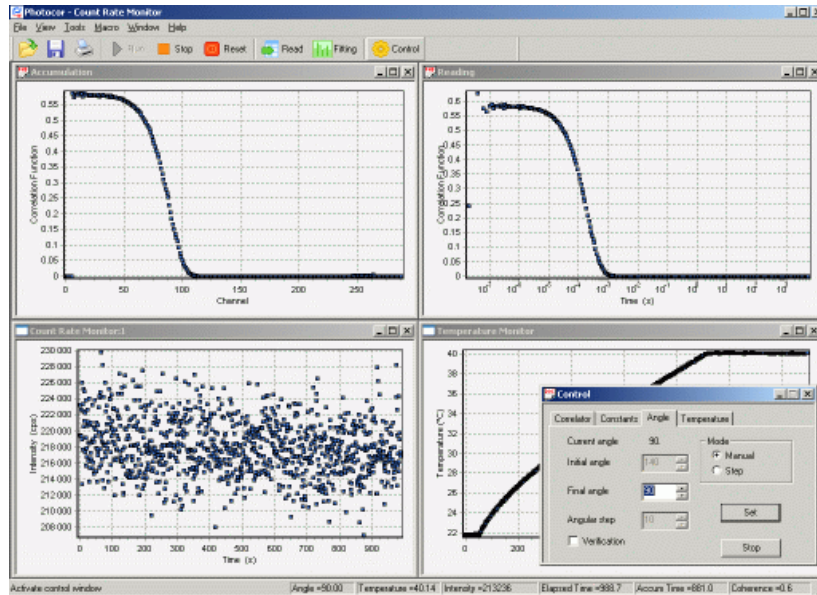


Figure 1.6: A screen shot of the Photocor-FC GUI.

Einstein-Stokes formula (see sections 1.3 and 2.3). The DynaLS software makes this analysis through a series of algorithms similar to Fourier Transforms although the actual process is not explicitly given to users. This software has a powerful advantage in that it allows the user to easily adjust the physical parameters and is capable of making computations on correlation functions with low signal-to-noise ratios or when the sample is non-monodisperse.

ALV correlator software is manufactured by ALV-GmbH, a German company that specializes in photon spectroscopy equipment. ALV software is capable not only of collecting correlation functions, but also of multiple in-depth analysis techniques. ALV has an advantage over other programs in allowing the user to fit the correlation function to multiple forms of an exponential decay and choose the best fit. This is important since DynaLS is only able to produce a probability distribution, and fitting the correlation function in a program such as Matlab is beyond most users

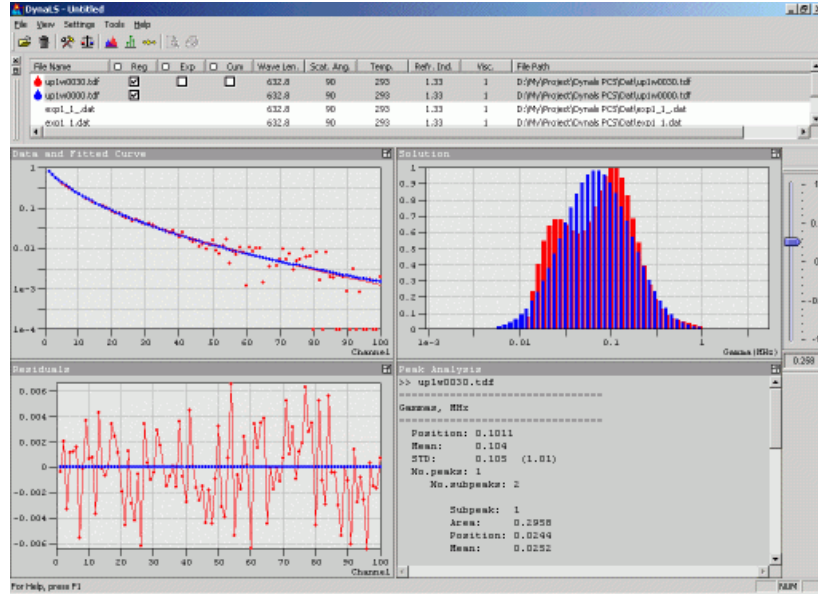


Figure 1.7: A screen shot from DynaLS software.

abilities. ALV does however have the disadvantage of requiring a more experienced user and is more difficult to automate for long or complex correlations.

It is important to note that while the different software programs enable users to better analyze correlation functions in different ways, the actual range of the relaxation times that can be recorded by each depends on the correlator hardware being used. With the correlators available to our laboratories, the Photocor correlators are able to measure faster relaxation times than the ALV correlator we have available.

Factors Affecting the Correlation Function: There are many different factors that can negatively affect the outcome of a DLS experiment. The most important of these is dust. In order to interpret the correlation function, it is a requirement that we allow it to decay from its maximum value, $\langle A^2 \rangle$, to its minimum value $\langle A \rangle^2$.

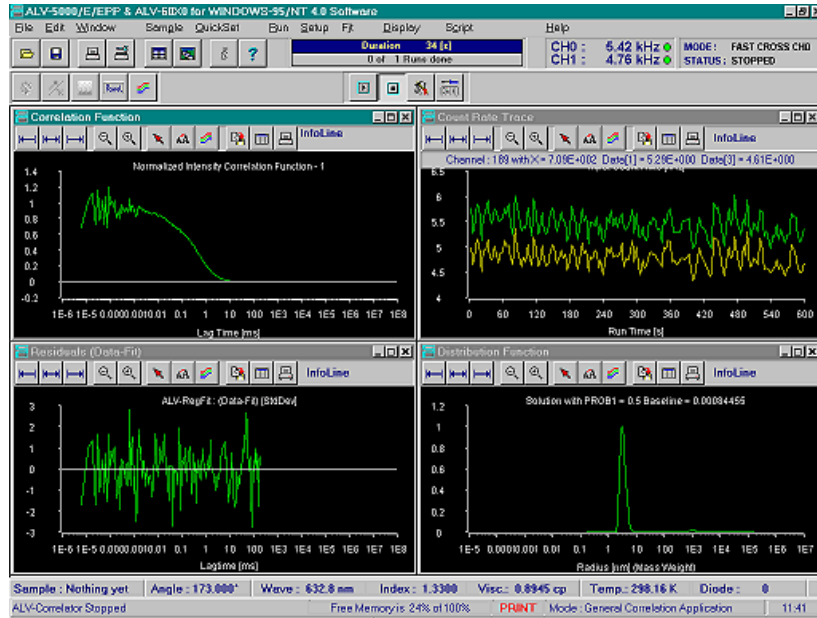


Figure 1.8: Screen shot of ALV software

Dust, or any large unwanted particle, will immediately destroy this maximum value and make the correlation function uninterpretable. There are other sources of unwanted light that could interfere as well. Aside from dust, the sample may have bacteria, air bubbles, or glass particles trapped in it from unclean receptacles or filtering equipment. Other sources of stray light may come from fluctuations in the laser intensity or large impurities in the sample cell. Any sort of non-equilibrium phenomena will also cause distorted light scattering. For instance, a temperature gradient in the sample may cause convection to occur. It may also be the case that a polymer being measured may aggregate in the solvent, producing large particles with very slow kinetics that were not anticipated. Due to these non-equilibrium processes, fluctuations will be present in the sample that were not anticipated and will negatively impact the correlation function. It may also turn out that the solvent

itself scatters an unwanted amount of light. While all solvent will scatter some light, in most cases the fluctuations that cause this light scattering are too small and too fast to interfere with the average measurement. It is only when the fluctuations of the solvent become large, due to approaching some sort of phase transition, that this may cause interference with the desired measurements. This is often a problem in binary solvents near a critical concentration, or in solvents that are near the melting or boiling points. For example, a binary solution may be near a critical point of de-mixing at certain concentrations and temperatures near room temperature. In these cases the critical fluctuations may be near the size of the particles that are being measured. One way to separate the contributions of the scattered light without changing the solvent would be to study the wave-number (q) dependence of the light scattering.

The next factors that can impair the measurement of a correlation function are interrelated: finite intensity and finite accumulation time. To deal with finite intensity we must understand which factors will affect the total energy that the detector encounters. A simplified equation to estimate the total energy incident on the detector is:²

$$E \sim \frac{I_o c_n}{\lambda^2 q^2}. \quad (1.17)$$

Where c_n is the concentration of the particles and I_o is the intensity of the incident laser. Hence, the total energy is largely a function of the laser intensity and the concentration, and is inversely proportional to q^2 . In order to increase the intensity

at the detector, we can either increase the concentration of the solute, increase the laser intensity, or decrease the scattering angle. As we go to extremely small scattering angles we will find that all terms become negligible compared to the concentration, and the concentration will dominate the overall scattering intensity.² In order to look at the required duration of the experiment, we can assume that we have a correlation function that decays as a simple exponential, $G(\tau) = 1 + e^{-\Gamma\tau}$. For this case, an experiment over a finite time period T , would then have a signal-to-noise ratio $S/N = (\Gamma T)^{1/2}$, where the decay rate $\Gamma = f(q)$.² Thus in order to increase the signal to noise ratio, one must either increase the total accumulation time, or increase q by increasing the scattering angle. Here we see the importance of tuning the wave number, q , in DLS experiments. In order to increase the intensity we can scatter from a small angle, but to reduce the noise in the signal we must increase the angle.²

A final factor that may damage the accuracy of the correlation function has largely been nullified by the increased capabilities of photodetectors, but will still be briefly addressed. Photomultipliers function by having electrons scattered from a crystal lattice, usually silicon-based, whenever a molecule in the lattice is impacted by a photon. Once a molecule releases an electron, that electron impacts other local electrons and creates a scattering effect that the photomultiplier detects as a count. This method involves some error due to what is called the "dead-time effect." The dead time effect is a result of the inability of the silicone lattice of the photomultiplier to scatter more electrons from a given area for a given period of time after being impacted by a photon. While better PMTs have largely reduced the effect to a level

not to create a significant error for most standard measurements, it is important to know the capabilities of any photodetector being used in case this becomes a factor.

CHAPTER 2

POLYMER CONFORMATIONS AND SIZE MEASUREMENTS BY DLS

2.1 Polymers in Aqueous Solutions

A hot topic in both chemical and biomolecular engineering is that of folding and unfolding of proteins. As a slow understanding is developed of self-assembling of proteins into larger structures, much of the ability of these formations to take place is accredited to the special shapes that proteins form when they fold. Proteins that are unfolded, or denatured, tend to aggregate and are thought to be the cause for many diseases of the human body. One step to understanding this phenomenon is to understand simpler cases in synthetic polymers. Normally polymer chains in a solvent will form a loose coil. Depending on the nature of the solvent, the length of this walk may vary. In a good solvent, one in which the monomers are more attracted to the solvent than to other monomers, the radius of the coil is thought to behave according to $R \sim N^{3/5}$, where N is the degree of polymerization.¹³ In poor solvents, the radius is much smaller as the coil tries to hide from the solvent and may be on the order of $R \sim N^{1/2}$. In a few rare cases however, the polymer may form a more complicated structure where intermolecular forces cause a polymer chain to form rod-like or helical structures. It is very common for this to be the case when a polymer has chiral components or is placed into some sort of chiral solvent.¹⁴ In the case study that follows, the observed polymer has no chiral components but exhibits helical conformations under certain conditions. What makes this case most

interesting is that this unique phenomenon occurs in one of the most commonly used commercial polymers.

2.2 Study of Poly(ethylene glycol) in Solutions

Our study in collaboration with Dr. Sandra Greer's research group at the University of Maryland has focused on a polymer known as PEG. PEG, poly(ethylene glycol), is a simple polymer chain made of units $[-O-CH_2-CH_2]$ terminated in an -OH group. A very close relative to PEG is Poly(ethylene oxide), PEO, which has the same monomer units but is terminated in an $-OCH_3$ group. In these chains the oxygen atoms can form hydrogen bonds making the chain hydrophilic.¹⁴ PEG is one of the most common polymers used commercially. It is used in paints, gels, lubricants, hair and skin products, medicines, and even food products. Being such a popular commercial product, PEG is available in a wide variety of molecular weights and polydispersities making it a widely studied polymer. It is widely accepted that when dissolved in water PEG forms the anticipated coils as most achiral polymers do. It has recently been shown, however, that PEG may form rod-like structures when dissolved in other solvents. This phenomena was found by Alessi *et al.*¹⁴ while trying to explain the fractionation of PEG into two phase solutions of isobutyric acid (IBA) and water found by Shresth *et al.*¹⁵ While IBA and water are generally mutually soluble at higher temperatures, IBA-water system with a large mass fraction of water will phase separate at low temperatures into a IBA-rich upper phase and a water-rich lower phase.¹⁶

One might expect that in a two-phase IBA-water solution, PEG would favor

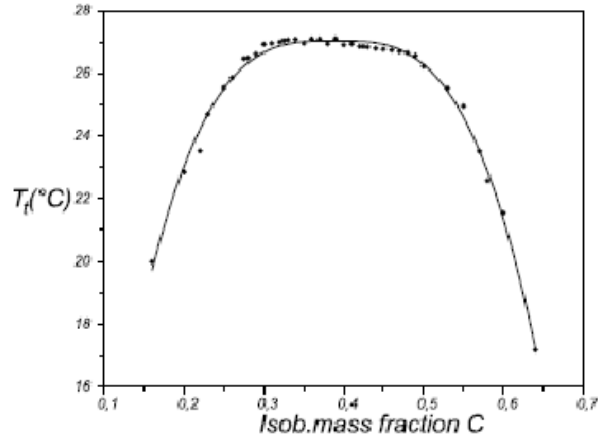


Figure 2.1: Coexistence curve of isobutyric acid and water according to Toumi *et al.*¹⁶

the water-rich phase since it is more soluble in water; this is called fractionation. Fractionation is a well-known phenomenon and usually the difference in polymer mass between the two phases is less than 10%.¹⁵ It was found with polydisperse samples of PEG that the smaller chains would remain in the upper IBA-rich phase while the larger chains would diffuse into the lower water rich phase. Overall 80% of the polymer mass would remain in the upper IBA-rich phase and the polydispersity of that phase was reduced.¹⁴ In order to find the reason for such odd behavior, Alessi *et al.*¹⁴ conducted Small Angle Neutron Scattering (SANS) experiments in order to determine the conformation of the PEG in each phase. They found that when in IBA, PEG samples with molecular weights 2.38×10^4 g/mol and higher formed a mixture of rods and coils at temperatures below approximately 60°C. Samples above approximately 60°C were found to contain only coils.¹⁴ The difference in the radius of gyration for 2.38×10^4 g/mol PEG was only about 8% between coil and rod, approximately 2.5 Å according to the SANS experiments.¹⁴ While this is not

a significant size difference, the most important results came from the polarimetry experiments. The polarimetry experiments showed no optical rotation in samples of PEG in water. Optical rotation was found in samples of PEG in IBA and confirmed that PEG did indeed take on a helical shape and that the number of helices slowly decreased as the temperature increased towards 60°C. Further experiments by this group showed that the PEG-IBA-water system follows Timmermans rule that if the polymer is soluble in both parts of a binary solution it should make the solution more stable and decrease the upper critical solution temperature (UCST).¹⁷ The group also showed that the introduction of urea into the sample, or the removal of all water from the IBA via molecular sieve would reduce or eliminate the concentration of PEG helices in the IBA.¹⁸ Together these results provide strong evidence that hydrogen bonding between trace amounts of water in IBA-PEG systems is the driving force for the coil-helix transition in PEG. This was further reinforced by experiments showing that in Poly(ethylene imine)-IBA systems, where the PEG -O- group has been changed to an -NH- group, the helices are even more stable.¹⁸ This is because the PEI amine group is able to create stronger hydrogen bonds than the PEG oxygen group. Because this is such an important and interesting phenomenon, we have decided to use light scattering to answer two questions: first, do the radius of gyration, R_g , measurements from the SANS data agree with the R_h measurement from light scattering; and second, can the coil-helix transition phenomena be seen by light scattering?

2.3 Dynamic Light Scattering in Poly(ethylene glycol) Solutions

DLS studies were conducted on PEG of molecular weights 2×10^3 and 2×10^4 g/mol. Samples were prepared both in solutions of water, IBA, and combined IBA-water solutions of 5%, 10%, and 20% water by volume. Water percentages were chosen in order to avoid large concentration fluctuations in the solution associated with the critical point of liquid-liquid phase separation. Experiments were conducted using a dual photomultiplier photon counting system with a 10 mW He-Ne laser as shown in figure 1.2. Temperature was controlled to one-tenth of a degree. PEG was received from Polymer Source (2KOH PEG) and Fluka (20KOH PEG) with measured polydispersity $M_w/M_n \sim 1.1$.¹⁴ The 20KOH PEG was then re-crystallized from methanol to increase its purity. De-ionized water was obtained from a water-purification system and IBA was obtained from Aldrich Chemical with purity 99.9%. No attempts were made to remove trace amounts of moisture from either the IBA or the PEG materials. Samples were prepared the day prior to the initial measurements and kept at an elevated temperature of 50°C when not being measured to aid in the dissolution of the PEG. Filtering was done using both 0.2 micron and 0.02 micron glass membrane filters.

While particle-size distributions are normally the easiest type of measurement to make with DLS, initial experiments found multiple difficulties inherent to the PEG-IBA-water system. Most notably the low solubility of PEG in IBA and small particle size only scattered at extremely small intensities that required long accumulation times for the calculation of a coherent accumulation function. To fur-

	5% H ₂ O	10% H ₂ O	20% H ₂ O
299° K	1.3934	1.3126	1.3903
311° K	1.3893	1.3890	1.3868
320° K	1.3849	1.3846	1.383
331° K	1.3814	1.3818	1.3803
343° K	1.3779	1.3782	1.3767

Figure 2.2: Measurements of the refractive index of IBA-water binary solution for three volume fractions of water at different temperatures.

ther compound the difficulties of the measurements, PEG also aggregates in IBA. The aggregates formed by the PEG in IBA were several microns in size and eventually would form visible precipitants. Such aggregates scatter with much higher intensities of light than the individual polymer molecules and resulted in correlation functions that were un-interpretable. This same problem was encountered during the SANS experiments noted above and prevented the research team from obtaining results at very small angles.¹⁴ The rate of aggregation was high enough that filtering with a 0.02 micron filter immediately prior to making measurements was not sufficient to allow for the accumulation of an unspoiled correlation function.

A final problem resulted from a lack of information available on the IBA-water system. In order to calculate the R_h from the Einstein-Stokes equation the viscosity and refractive index must be known accurately. Refractive index measurements were made with a Reichert Abbé refractometer with temperature control provided by a water circulating bath controlled to 1/10 degree Kelvin. The results are displayed in figure 2.2.

Partial viscosity data for the IBA-water system have been reported by Ourfelli *et al.*¹⁹ The data were fitted to the Arrhenius formula and extrapolated over the experimental temperature range. These data were then compared with an interpolation of the viscosity data for pure water and IBA as published in the CRC handbook.²¹ It is important to note the difference between the interpolated viscosity and the published results. The actual viscosity of the system is much larger than what would have been assumed by using an interpolated viscosity of the system, likely a result of hydrogen bond interactions. A two-times difference in the viscosity used to calculate the hydrodynamic radius would have erroneously yielded a solution twice different from the actual R_h . Figure 2.3 shows the values for the pure fluid systems as well as the Arrhenius fits to the actual viscosity data for the 5% and 10% water systems.

After conducting numerous initial tests, experiments with PEG in pure IBA were found to have extremely high rates of aggregation that prevented any accurate measurements. To combat the aggregation of the polymer, new software was needed from Photocor. Photocor v38 was made available to our research group from the company to use for testing. The software provided the unique capability to break up the long accumulation times of a correlation function into many short accumulation times and then sum them together to compute a final correlation function. In the process of computing the final correlation function, Photocor v38 is able to discard any of the short segments in which the intensity deviates from a preset allowance of the average intensity. This allows for the removal of intensity spikes caused by aggregates that would otherwise spoil the correlation function.

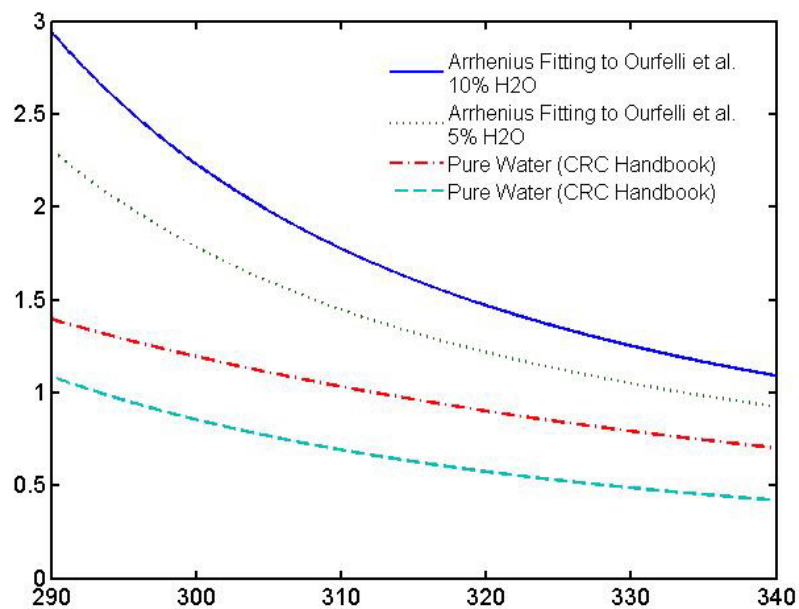


Figure 2.3: The shear viscosities of IBA, Water, and IBA-water binary solutions as a function of temperature. The plots for the pure liquids are made from the Arrhenius equation given in the CRC handbook.²¹ The plotted lines for the binary liquids are Arrhenius fits to data from Ourfelli *et al.*¹⁹ made using Matlab.

The measured correlation functions were significantly improved by the use of the new software. An example is provided in figure 2.4, where the data points for the correlation function are shown by open circles. While improved, the correlation function in figure 2.4 still exhibits some noise as a result of the low signal-to-noise ratio. Given an infinite accumulation time, this correlation function should come together to fit a single exponential decay if the sample is monodisperse and the particles are non-interacting. In figure 2.4 the correlation function has been fitted with the aid of Matlab software to the best possible single exponential decay which has a relaxation time $\tau = 0.0368\text{ms}$. For relaxation of diffusion fluctuations we can find the diffusion coefficient from:

$$\tau = \frac{1}{Dq^2}. \quad (2.1)$$

This equation with the Einstein-Stokes formula, equation 1.4, allows us to determine the hydrodynamic radius.

The second available method to analyze the correlation function is by using the DynaLS software described in Chapter 1. This software gives a particle-size probability distribution that is characterized by a position, a mean, and a standard deviation. The position provides the most probable particle size for a given correlation function. The probability distribution functions for PEG in three different solvents are given in figures 2.5, 2.6, and 2.7. While the uncertainty in the DynaLS analysis for these correlation functions is relatively large, the probability distributions better account for the noise in the correlation functions than the fit to the

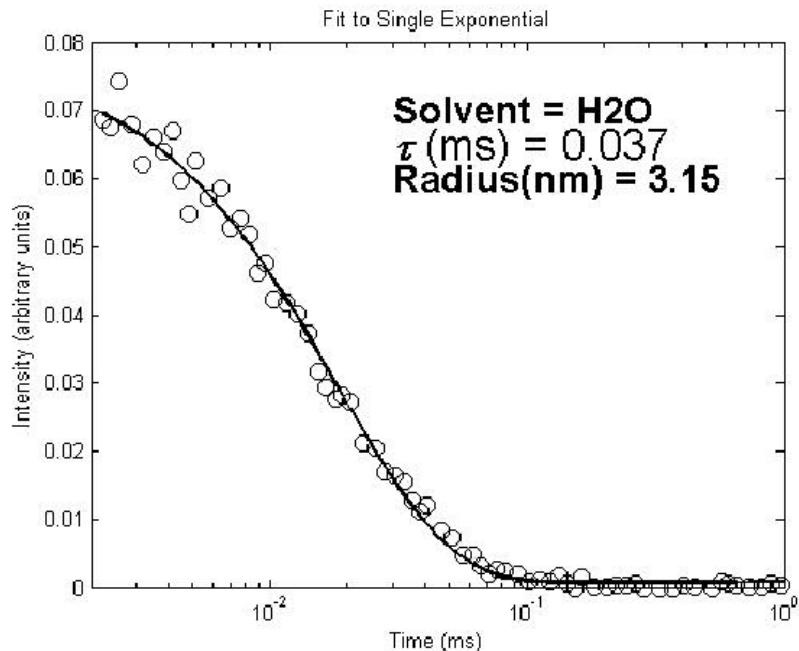


Figure 2.4: The measured correlation function for 20KOH PEG in water. The solid line is a single exponential fit to the correlation function computed by Matlab.

single exponential decay. Thus, for the purpose of comparing with SANS results, the DynaLS results will be used rather than the results from Matlab fitting process.

A summary of the results is given in figure 2.8. Comparing R_h from light scattering to that from the SANS data R_g we found that the ratio $R_h/R_g \sim 0.76$ using the R_g obtained by Alessi *et al.* and Norman *et al.* and the R_h from the DynaLS analysis. This is in excellent agreement with the only relation available for comparison provided by Devanand and Selser²⁰ who developed a relation from static and dynamic light scattering in PEO with $M_w \geq 10^5$. Devanand and Selser fit static light-scattering data to obtain the relation $R_g = 0.215M_w^{.583 \pm .031} \text{ \AA}$ and then fit dynamic light scattering data to obtain the relation $R_h = 0.145M_w^{.571 \pm .009} \text{ \AA}$. Using these relationships for R_h and R_g in PEO we predict $.040 < R_h/R_g < .088$. To

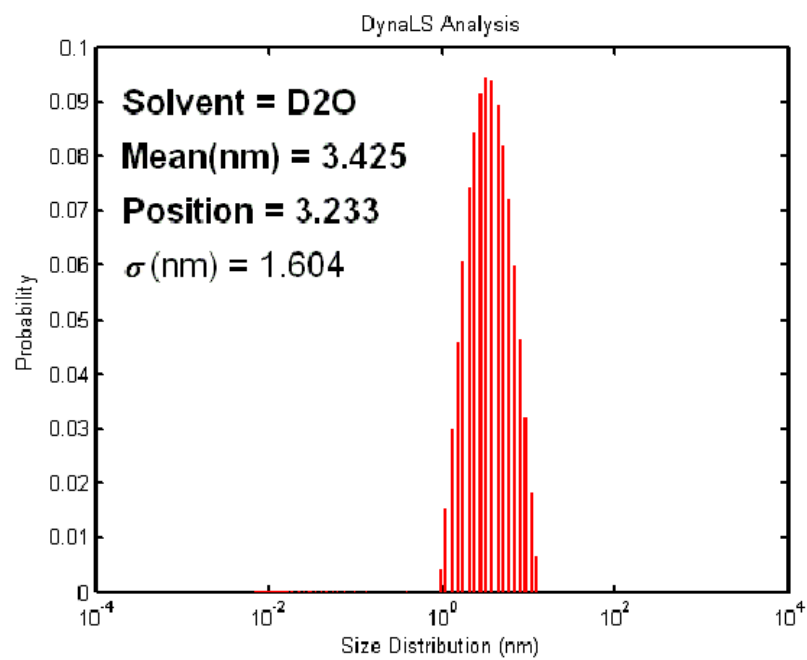


Figure 2.5: DynaLS computed probability distribution function for PEG in D2O.

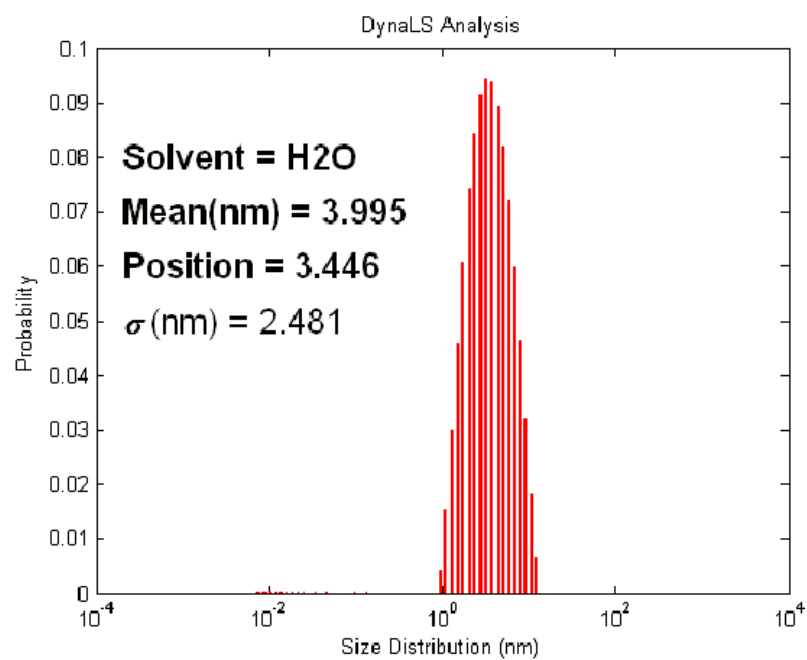


Figure 2.6: DynaLS computed probability distribution function for PEG in H2O.

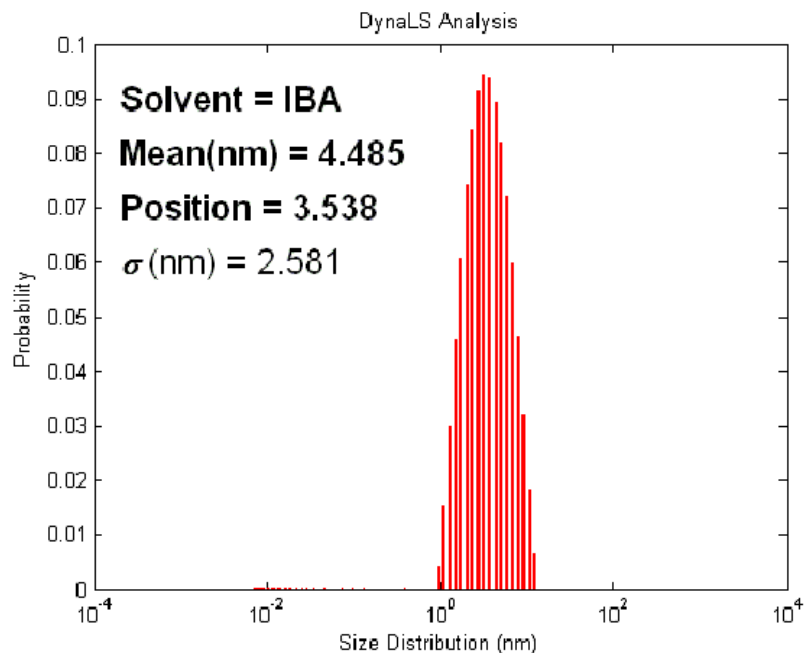


Figure 2.7: DynaLS computed probability distribution function for PEG in IBA.

ensure that the results were not an effect of the different solvents (SANS required deuterated solvents), the R_h of PEG was also measured in D_2O for comparison. The viscosity and refractive index data for D_2O were found in the CRC Handbook²¹ and Lewis *et al.*,²² respectively. While the results from the measurements in D_2O did tend to be slightly smaller than measurements in water, the difference falls well within the accuracy of the measurements and no conclusive statement can be made about the effect of the stronger hydrogen bonding on the polymer coil size. It is still very much a possibility that the stronger hydrogen bonding effects present in D_2O would affect the size of particles measured by SANS. However, any difference in the size of the polymer coil resulting from stronger hydrogen bonds in the solution would be of the order of 10% and would not be the sole cause of the size differences seen in figure 2.8. Instead, the value of the ratio R_h/R_g is likely a result of the assumptions

	$\langle R_h \rangle$ DynaLS (nm)	$\langle R_h \rangle$ Matlab (nm)	$\langle R_g \rangle$ from SANS (nm)
H ₂ O	3.45±2.5	3.15±0.45	N/A
D ₂ O	3.23±1.6	3.02±0.3	4.3±.1
IBA	3.54±2.6	3.16±0.45	4.6±.1*

Figure 2.8: Table of radius measurements for 20KOH PEG in solution by different methods.

inherent to each type of measurement. Light-scattering models for determining the R_h assume that the measured particles are non-interacting spheres, and thus yield a radius for a sphere that moves at with the same rate of diffusion. SANS relies on several complex models, each unique to the type of measurement being made. No relation is currently available to reconcile the results obtained by the two different experimental techniques. As measurements at the nano- and meso- scales become more and more important, a model will eventually have to be developed in order to allow for accurate comparison of SANS and DLS results.

Measurements were also made at various temperatures in order to ascertain whether or not a change in the conformation of PEG can be detected with DLS. In order to detect such a small change as is anticipated in the aqueous PEG system an extremely large scattering angle needs to be used (see Chapter 1). A special mirror apparatus was assembled to alter the path of the beam and create an otherwise unachievable scattering angle of 168°. As a result of the large angle heterodyning occurred and affected the accuracy of the system while the precision was increased. As a result it was possible to make repeatable measurements with small standard deviations, but the measured R_h appeared smaller due to the stray light of the inci-

dent beam entering the photomultiplier. Even with the extreme angle, the precision of the DLS instrument could not be tuned such that the temperature dependence of PEG could be measured with a standard deviation less than 0.5 nm. Because of this, it was determined that the available DLS technology could not detect a size change of 0.25 nm as is expected from the PEG conformation change.^{14, 17}

There are several possibilities for dynamic light scattering not being able to detect the size change in the polymer. One possibility is that because the helix conformation of the polymer exists in equilibrium with coils of the polymer, the effect on the $\langle R_h \rangle$ is minimized. Based on the results from the polarimetry experiments outlined above, one would expect the average radius of gyration to be largest at the lowest temperature, where the largest number of helices exist, and then reduce to a minimum at the highest temperature, where the highest number of coils exist. It may also be that the size difference is just simply too small to be distinguished by light scattering, particularly when M_w/M_n already introduces a 10% error. Finally we can question whether we should expect to see any change at all considering significant the difference seen between the R_g and the R_h shown in table 2.8. If there is only an 8% change to begin with in the R_g when the coil changes to a helix, this would translate to a much smaller change in the smaller hydrodynamic radius. Also, because the hydrodynamic radius measures only the way the particle move in the solvent, this may not change at all with a change in the conformation.

Several conclusions can be drawn from this study of PEG in aqueous solutions. First, while water may be a fair solvent for small M_w PEG at low concen-

trations,²³ both water and IBA drive PEG to cluster and aggregate in solution and make for a difficult system in which to conduct DLS measurements.^{14, 17, 23, 24} Second, there is a clear difference between measurements made with SANS and DLS. While the relation given by Devanand and Selser²⁰ seems to hold for the case of PEO and PEG, it is likely to be different depending on the nature of the solvent and hydrophobic effects of the system. Finally, it appears that for such a small change in conformation, DLS is not the best tool to observe such a phenomenon. In order to observe a change in conformation by using DLS, either a larger polymer should be studied in order to increase the intensity of the scattered light, and/or a more powerful laser should be used to increase the scattering intensity.

CHAPTER 3

PROTEIN AGGREGATION KINETICS BY DLS

3.1 Protein Folding and Aggregation

Currently the scientific community is making great efforts to understand the folding and unfolding of proteins. Not only is it important to help cure disease, but there is also a real possibility that a thorough understanding of the mechanisms behind folding will allow future engineers to build new proteins and nano-structures. When proteins denature, aggregation is often soon to follow. Because aggregation leads to the creation of larger structures and sometimes even visible precipitants, it can be easier to study the aggregation rather than the unfolding of proteins. By studying the kinetics of aggregation we can learn about the driving forces behind the unfolding of the protein that led to the aggregation. It is also important to understand the bonds that keep proteins together. Proteins, like polymers, are made up of many subunits. By breaking apart the subunits into monomers we can understand the nature of these bonds. The experiments described in this chapter will attempt to explore both kinetics of aggregation as well as the driving forces of bonding.

One previous study of aggregation and driving forces was conducted on tobacco mosaic virus (TMV) using DLS.²⁵ In the study by Panyukov *et al.*,²⁵ two different methods were used to induce aggregation of TMV protein coat. The two different methods, increased temperature and addition of a surfactant, surprisingly showed two different types of aggregation. In the first case the protein was dissolved

in water and heated to 52°C. The aggregation was measured by a Photocor DLS setup similar to the basic setup described in chapter one of this thesis. Measurements showed the change in the hydrodynamic radius of particles present in the solution as well as the increase in the intensity of the scattered light. The results showed that the "start" aggregates on the order of ~ 25 nm were present almost immediately in the elevated temperature solution. After a short time "basic" aggregates appeared on the order of ~ 100 nm. These aggregates then grouped together to form "super" aggregates that were large enough to precipitate from solution, >1000 nm.²⁵ The group was able to show that the basic aggregates formed the super aggregates by first heating a sample to 52°C and then cooling it quickly to 25°C and watching to see if the super aggregates still formed. The formation of the basic aggregates nearly ceased while the number of super aggregates increased significantly. A chaperonin protein was then added to the solution to see if the process was reversible. The process was deemed irreversible as the addition of the chaperonin protein had no effect on the aggregation process when aggregation was induced by increased temperature.²⁵

In the same study by Panyukov *et al.* aggregation was also induced by the addition of cetyltrimethylammonium bromide (CTAB) which is a cationic surfactant. The addition of CTAB even at small micro-molar quantities was found to start the aggregation process in TMV PC.²⁶ When DLS experiments were performed on the CTAB aggregated protein, it was found that only a single type of aggregate was formed which increased in size over time. No super aggregate was found to form from the collection of smaller basic aggregates as was found with temperature induced

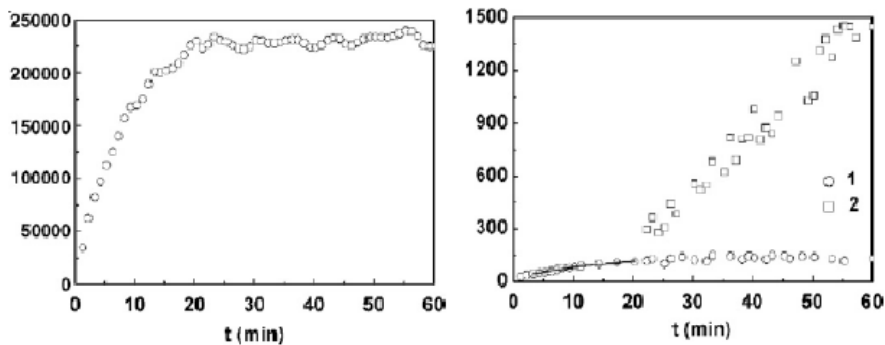


Figure 3.1: Results from TMV study by Panyukov *et al.*²⁵ Left: Intensity increases as a function of time until it reaches a critical level where the rate of precipitation is equal to the rate of formation of new aggregates. Right: The rate of gyration increases linearly at short time before splitting and forming two separate types of aggregates.

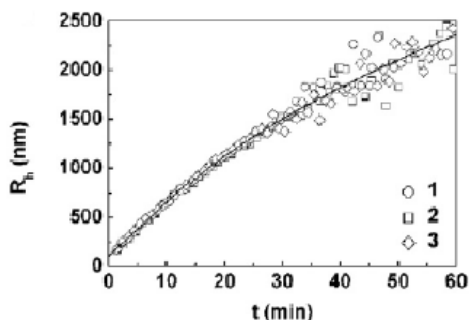


Figure 3.2: Results from TMV study by Panyukov *et al.*²⁵ show the increase of the radius of gyration with time of aggregates when three different molarities of CTAB are added to the solution at 25°C

aggregation.²⁵ It was also found that the surfactant aggregation was reversible.

Other studies on aggregation have also utilized light scattering to measure the size of aggregates. In a study by Militello *et al.* the aggregation of bovine serum albumin (BSA) was observed.²⁷ It was found that changing by the pH of a sample of BSA nearer to its isoelectric point (pI) the BSA would begin to aggregate. Small changes in the pH (from pH=7.4 to pH=7.2) would result in reversible aggregation with no super aggregates similar to the aggregation of TMV PC with CTAB. A large

change in pH (from pH=7.4 to pH=6.2) resulted in irreversible aggregation with the formation of super aggregates and precipitants similar to that found in TMV PC aggregated by a change in temperature.²⁷

In an experiment by Schuler *et al.* in Germany the aggregates of human transferrin receptor were measured as the protein aggregated at temperatures between 20-47°C.²⁸ It was found that basic aggregates formed at temperatures above and below the human-body temperature, but that at temperatures above 47°C, super aggregates formed that they called fractal aggregates. They were able to take pictures of the aggregates and noted that the basic aggregates formed dendritic structures of similar size which were in coexistence with the larger fractal aggregates. A similar experiment on α -lactalbumin showed results suggesting intermediate aggregates,²⁹ while a study by Khanova *et al.* found steady growth of aggregates with no intermediary.³⁰

These studies, taken along with many others that are not mentioned here, seem to suggest two types of aggregation taking place. In one case reversible intermediate aggregates conglomerate into larger super aggregates which tend to precipitate and are not reversible. In another case aggregates grow continually from start aggregates and may also be reversible. In a study by Speed *et al.*³¹ they conclude that there are in fact three different types of aggregation kinetics: particle-cluster polymerization, where aggregates grows by the addition of individual units; cluster-cluster polymerization, where aggregates grows by the addition of randomly sized multi-particle units; and nucleation-growth kinetics, where the individual units combine slowly to form a nucleus which then rapidly aggregates with other clusters to

form precipitous aggregates.³¹ The third type of aggregation is a combination of the first two. Each of these three types of aggregation can potentially be described by using kinetic models for polymerization. The difficulty, however, remains in that aggregation processes are rarely thermodynamically reversible and often require the presence of a chaperonin protein in order for proteins to be refolded.³² This combined with the fact that the inter- and intra- molecular forces that drive the aggregation process are not fully understood leave much to be desired in current models of protein aggregation.

3.2 Chaperonin Protein GroEL

For our study, in cooperation with Dr. Lorimer's research group of the University of Maryland Department of Chemistry and Biochemistry, we chose to study the well-known protein GroEL.³³ GroEL, originally known as protein cpn60, is a homotetradecamer extracted from E-coli bacteria. It's purpose *in vivo* is to assist in the folding and unfolding of other proteins and is thus referred to as a chaperonin protein.³³ The fourteen units that make up the tetradecamer are assembled into two hollow rings that stack onto one another. Each monomer unit then has three distinct regions that are each thought to have a different role in the folding and activity of the protein. The upper portion of each monomer is the apical region, while the area of each monomer where the two ring stack is the equatorial region.^{34,35} The apical and equatorial regions are connected by an intermediate region. The apical region is credited with the binding other proteins to GroEL. The equatorial region is thought to be where the monomer-monomer interactions take place.³³ GroEL

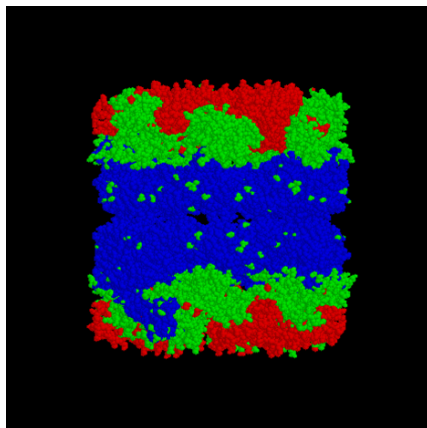


Figure 3.3: Computer generated image of GroEL viewed from side.³⁶

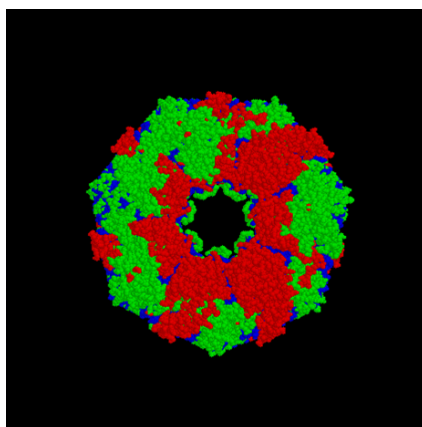


Figure 3.4: Computer generated image of GroEL when viewed from an end.³⁶

has been heavily studied for folding and unfolding interactions. Most studies have used guanidine hydrochloride (GdHCl) and urea both of which are very popular denaturants.

One of the first experiments by Price *et al.* found GdHCl to be a very effective denaturant for GroEL even at low concentrations.³⁷ Later experiments by Mizobata and Kawata used static light scattering as a measurement tool and GdHCl as a denaturant. From this experiment some evidence was found in support of the idea of an intermediate protein conformation that takes place during the denaturing

of GroEL.³⁸ More recent studies have been conducted to in an attempt to prove that the unfolding of GroEL is a multi-step process. A study by Chen and Smith used both urea and GdHCl and found that urea can be used to separate the tetradecamer into monomers.³³ Chen and Smith also found evidence that low molarities of GdHCl will start the unfolding of GroEL apical and intermediate domains while higher molarities of GdHCl will denature the entire protein.³³ This would seem to prove the multi-step denaturing theory, however, the results of their CD experiments were inconclusive.³³ The theory discussed in part one of this chapter heavily supported the idea that most proteins have intermediate folding conformations where they are most vulnerable to aggregation and hence require chaperonin proteins to prevent and reverse the aggregation process.³¹³²

The purpose of our study of GroEl was to attempt to discern the mechanism of aggregation of GroEl when precipitated by acetone. It is common practice to use acetone in biochemistry laboratories to precipitate GroEl from solution. It is thought that this process is reversible, although little research has been done to show the mechanism by which this precipitation occurs. Some research suggest that acetone allows for the exchange of monomeric units between GroEl proteins and that it causes the unfolding of the apical region of the monomeric units which leads to aggregation. Acetone is a strong aprotic solvent that is capable of forming hydrogen bonds. When water and acetone are mixed in a binary system, the water behaves differently as the acetone interacts with the water-water hydrogen bonds.³⁹ It is no surprise then that the acetone would effect the protein folding when most protein folding is driven by hydrophobic reactions as well as hydrogen bonding.

3.3 Aggregations Processes of GroEl Studied by DLS

DLS studies were conducted on GroEl in both pure water and acetone-water binary solutions. Binary solutions were of 5%, 10%, 15%, and 20% acetone by volume in water. Concentrations of GroEl ranged from 1.5 μM to 6 μM . GroEl protein was purified after extraction from *E.coli* bacteria in the biochemistry laboratories at the University of Maryland College Park. The buffer and solution were equilibrated to the desired temperature in the DLS apparatus with temperature control at $\pm 0.1^\circ\text{C}$. When the desired temperature was reached for the solution, the protein was added to the sample cell and gently stirred. Light-scattering measurements were then taken using the basic setup as described in chapter one of this thesis. Standard Photocor-FC software was used for the accumulation and calculation of the correlation function.

It was determined that the hydrodynamic radius (R_h) of the GroEL protein at 37°C was approximately $9.5 \pm 0.3 \text{ nm}$ when measured in pure water with buffer. This was determined by fitting the correlation function to a single exponential decay with the Matlab software, as well as by using DynaLS software to compute the size distribution probability function and conducting an analysis of the residuals. The hydrodynamic radius is in excellent agreement with the literature. The accepted dimensions of GroEL from the crystal structure are those of a cylinder with diameter 13.7 nm and height of 14.6 nm.^{34, 40, 41, 42} The measured radius of gyration (R_g) from SANS is smaller in this case compared to the R_h likely due to the geometric shape of the protein. The reported R_g from SANS is approximately $6.5 \pm 0.2 \text{ nm}$.^{40, 41, 42, 43}

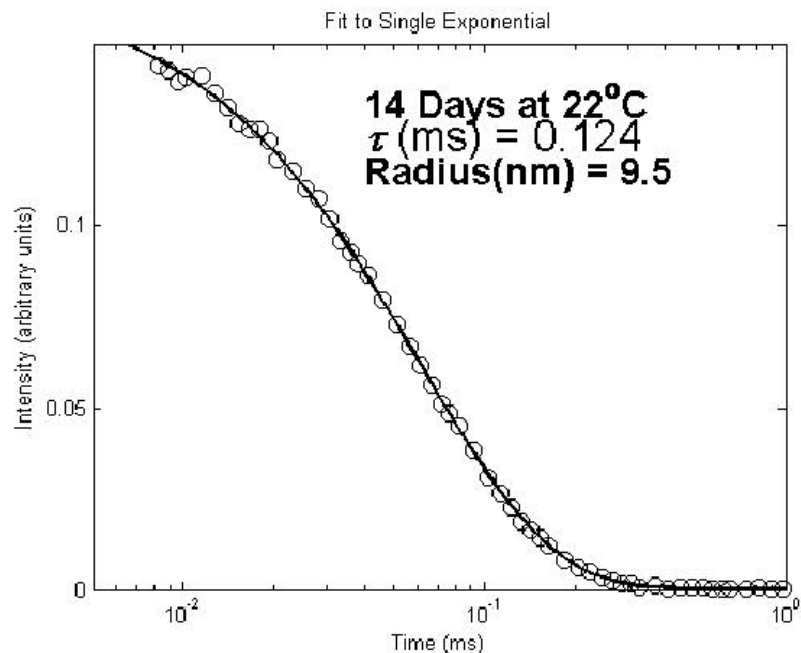


Figure 3.5: The correlation function measured from a sample of GroEL after two weeks at 22°C.

It was also determined from preliminary experimentation that the stability of the GroEL protein in *vitro* is quite extraordinary. It was found that a protein sample in buffer was stable for well over a month when kept at either room temperature or also when incubated at 37°C. Samples of the protein with buffer were kept at both room temperature and 37°C for several weeks and were measured every other day to determine if aggregates formed or if the size of the protein changed due to denaturing or dissociation. It was found that no size change was evident even after 8 weeks. The samples were also heated to temperatures of 55°C, incubated for several hours, and cooled back down to room temperature. No size change was evident even after this treatment.

Upon the addition of acetone to the solution, aggregates began to form im-

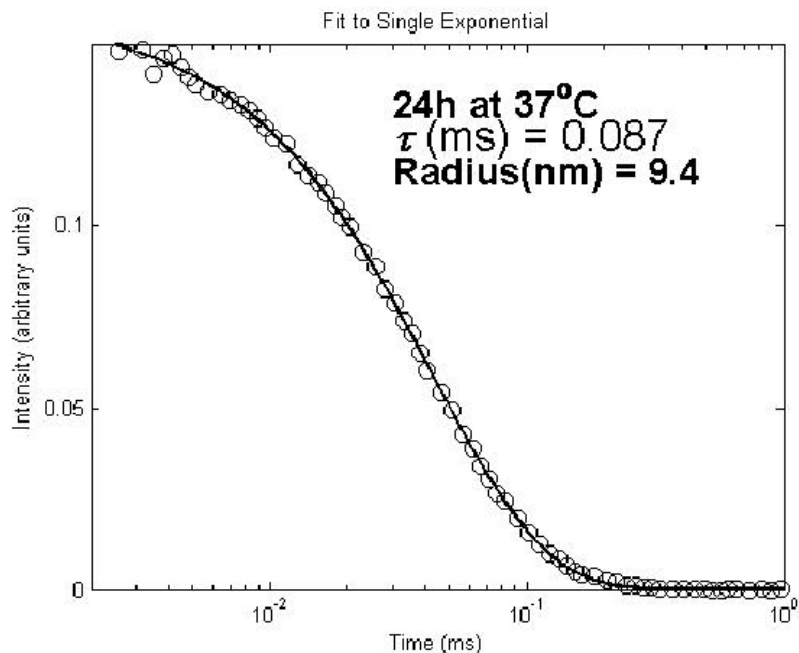


Figure 3.6: Correlation function for GroEL measured at 37°C.

mediately. As aggregates formed the intensity of the scattered light also began to increase. It was found that the change in intensity of the scattered light was directly related to the aggregation process taking place. The aggregation process was controlled by both the concentration of the acetone as well as the concentration of the protein. The concentration of the acetone was found to determine the size of the aggregates and whether the formation of super aggregates took place. The formation of superaggregates was not observed in the samples with concentrations of 15% or less acetone. The concentration of the protein on the other hand was observed to determine how quickly the maximum intensity was reached. This means that the time it took for the rate of aggregation to equal the rate of precipitation was increased with the concentration of the protein. This suggests that the rate limiting factor, protein diffusion in this case, can be controlled by controlling the

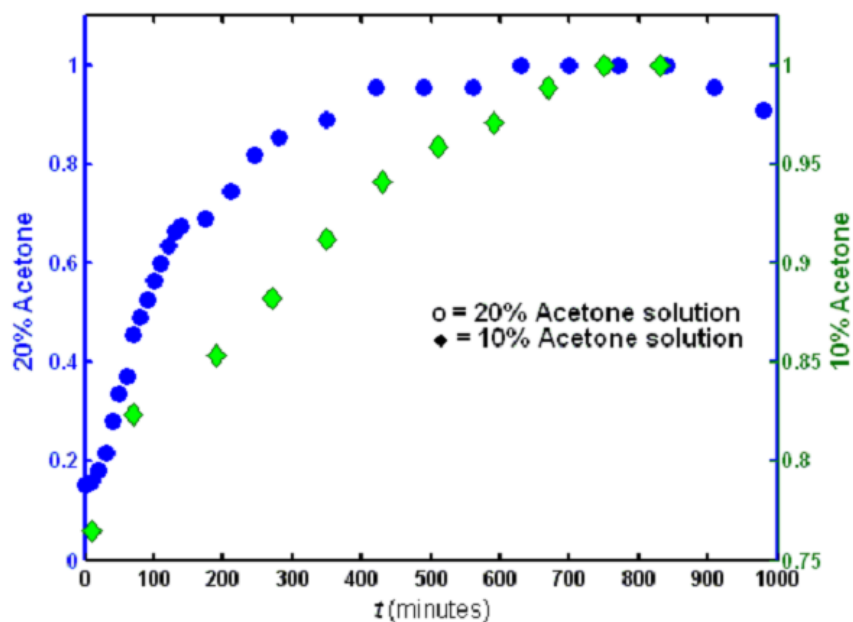


Figure 3.7: A plot of the normalized intensity of scattered light versus time. The normalized intensity scale for the 20% acetone solution (circles) is on the left y-axis. The normalized intensity for the 10% acetone solution (diamonds) is on the right y-axis.

concentration of the protein.

In figure 3.7 the normalized intensity of 20% acetone and 10% acetone solutions are compared when they contain the same concentration of protein. The normalized intensity for the 20% solution is marked on the left y-axis and normalized intensity for the 10% solution is marked on the right y-axis. While it appears that the time required to reach the maximum intensity is equal for both samples, the 20% acetone solution exhibits a five-fold increase in scattering intensity while the 10% solution exhibits only a 30% increase in scattering intensity. Again, the formation and precipitation of superaggregates was not observed in the 10% acetone solution suggesting that the increase in scattering intensity was due primarily to the

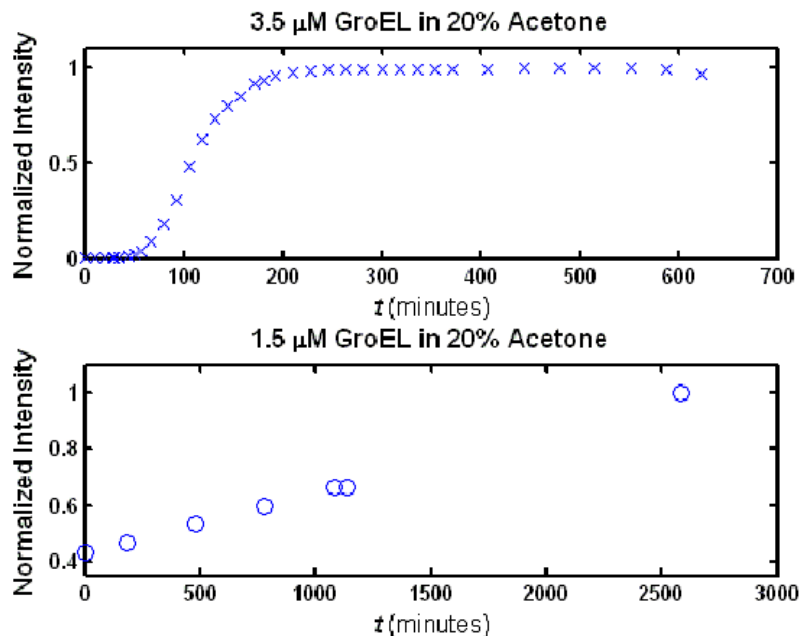


Figure 3.8: Normalized intensity plots for a 3.5 μM GroEL concentration sample (top) and 1.5 μM GroEL concentration sample (bottom) both in 20% acetone solution.

formation of start or basic aggregates.

In figure 3.8 two normalized intensity plots are shown for samples containing 3.5 μM (top) and 1.5 μM (bottom) concentrations of GroEL protein in 20% acetone water solutions. Fewer data points are available for the 1.5 μM solution due to the slow kinetics exhibited by the sample. However, the data still clearly show that intensity in the 1.5 μM sample reached a maximum long after a maximum intensity was reached in the 3.5 μM sample and suggests that the rate of aggregation of GroEL in the acetone-water system is only controlled by the ability of the protein to diffuse and interact with other protein in the sample.

Once acetone is added to a protein sample it becomes difficult to determine the size of the individual GroEL proteins. This is due to the almost immediate

appearance of aggregates in the solution. Once aggregates begin to form in the solution the ability to determine the size of the smallest particles is interrupted by the high intensity scattering of the larger aggregates in the sample. This made it nearly impossible to tell whether there was a change in size of the GroEL protein due to the denaturing of the protein as a whole or whether there was a dissociation of the protein monomers. However, it was not necessary to be able to accurately measure the size of the individual GroEL protein in order to be able to measure the size of the aggregates. By means of the DynaLS software program it was possible to break the correlation function into a particle size distribution and show the formation of start, intermediate, and super aggregates as is shown in figure 3.9. While it appears in figure 3.9 that the start aggregates disappear after a certain period of time, this is actually a result of the masking effect by the high intensity scattering of the larger aggregates.

The data for figure 3.9 is obtained from the same measurements used to provide the static light scattering data for the 3.5 μM sample in figure 3.8. Note that upon comparison of static and dynamic light scattering data the appearance of the intermediate aggregate coincides with the maximum slope in the static light scattering curve around $t = 50$ min. Also the appearance of the superaggregates coincides with the slight drop in intensity at $t = 600$ min suggesting that precipitation is occurring.

From these results we can draw four compelling conclusions. One, GroEL is quite stable *in vitro* even at a wide range in temperatures. Second, the aggregation seen in 20% acetone solutions is very similar to that observed by Panyukov *et al.*²⁵ in

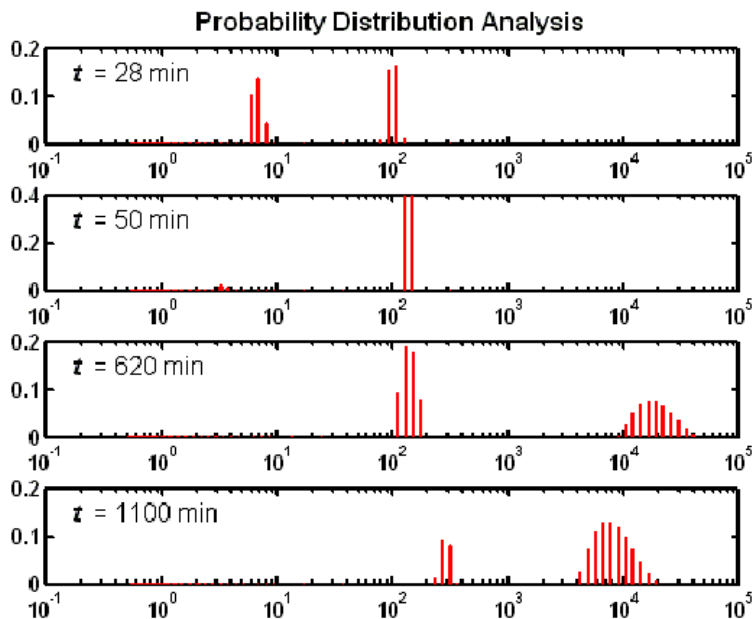


Figure 3.9: Four probability size distributions from DynaLS analysis of correlation functions taken at elapsed times for the $3.5 \mu\text{M}$ GroEL concentration sample with 20% acetone.

TMV CP when precipitated by a change in temperature. Thus, based on the results found by Panyukov *et al.*²⁵, it is very likely that this sort of large aggregate formation and precipitation is irreversible. Third, along the same lines, the aggregation found in 10% acetone solutions is very similar to that observed by Panyukov *et al.*²⁵ when TMV CP was aggregated by CTAB and by Militello *et al.*²⁷ when a small change in the pH caused aggregation of BSA. It is very likely then that the aggregation observed in 10% acetone solutions is reversible. Finally, the aggregation of GroEL in acetone solutions can be described by the nucleation-growth kinetics reported by Speed *et al.*³¹, which involves the growth of intermediate aggregates by the collection of individual monomers and then the formation of super aggregates by the clustering of intermediate aggregates. Further experimentation on this system may be useful

to quantify the aggregation kinetics for GroEL. This may eventually allow for an unified theory of aggregation kinetics.

CHAPTER 4
DYNAMICS OF PRE-TRANSITIONAL FLUCTUATIONS IN A
LYOTROPIC CHROMONIC LIQUID CRYSTAL

4.1 Fluctuations in Pure Fluids, Binary Mixtures, and Polymer Solutions

In Chapter 1 the idea of critical opalescence was briefly discussed. When a fluid is approaching a phase transition, fluctuations of density or concentration become larger and larger in that fluid. Eventually as the fluid comes very near to the critical point, the fluctuations are strongly scatter light, making the fluid appear opaque. In one-component fluids and binary mixtures there is a single length scale that characterizes the size of the fluctuations, namely the correlation length, ξ . When the temperature of the fluid is far from a critical temperature, ξ is of the order of intermolecular size; as the fluid approaches a critical temperature ξ can become quite large, reaching hundreds of angstroms.⁴⁴ The time required for a fluctuation to relax at a given instrumental length scale is τ_q ; a function of both the rate of diffusion and the instrumental scale, q . Thus:⁴⁶

$$\tau_q = \frac{1}{D(q, \xi)q^2}. \quad (4.1)$$

The diffusion coefficient $D(q, \xi)$ is composed of two contributing diffusion coefficients of the sum $D(q, \xi) = D_c + D_b$, where D_c is the critical contribution to the diffusion coefficient and D_b is a background contribution to the critical coefficient.⁴⁵ As $q \rightarrow 0$ and as $T \rightarrow T_c$, the critical contribution of the diffusion coefficient is described by the Stokes-Einstein diffusion relation:⁴⁷

$$D_c = \frac{R_D k_B T}{6\pi\eta\xi}, \quad (4.2)$$

where η is the shear viscosity of the system. The dynamic amplitude ratio, R_D , in first approximation is equal to unity.⁴⁶ More importantly, the correlation length, ξ , is a strong function of temperature following the power law $\xi = \xi_o \epsilon^{-\nu}$ where $\epsilon = (T - T^*)/T$.⁴⁷ The exponent⁴⁷ ν has a value of 0.630, while the value of ξ_o is system dependent; T^* is the second-order transition temperature.

Thus the diffusion coefficient associated with critical fluctuations corresponds to a single exponential decay time present in the time-dependent intensity correlation function of simple fluid mixtures. Polymer solutions, however, tell a more complex story. Critical dynamics in polymer solutions is very instructive to understanding dynamics in liquid crystals. This is because, as in polymer solutions, liquid crystals exhibit multiple dynamic modes associated with their pre-transitional fluctuations. The reason multiple modes appear is the existence of multiple mesoscopic length scales in the solution. In polymers, two length scales appear: the first, a correlation length of critical fluctuations of concentration; and the second, the radius of gyration of the polymer molecules.⁷⁵ The mesoscopic length scales in polymers can be tuned. The radius of gyration of polymers changes with the molecular weight of the polymers, while the temperature of the system makes the correlation length variable.⁴⁶ It was predicted by Brochard and de Gennes that polymer entanglements, dependent on the radius of gyration, would lead to a coupling of the viscoelastic and diffusive dynamic modes which are both present in polymer solutions, particularly

at high molecular weights.⁴⁷ By increasing the polymer molecular weight, the radius of gyration grows and may become larger than the correlation length associated with the critical fluctuations of concentration. The appearance of two dynamic modes in polymer solutions has been observed by several research groups including Tanaka *et al.*,⁴⁸ Adam and Delsanti,⁴⁹ Jian *et al.*,⁵⁰ and Nicolai *et al.*⁵¹ The most recent and in-depth study of this phenomenon was by Kostko, Anisimov, and Sengers on polystyrene solutions⁴⁶.

Using the same light scattering equipment described in Chapter 1 of this thesis, Kostko *et al.* studied multiple molecular weights of polystyrene in cyclohexane with radii of gyration varying from 12 to 89 nanometers. They observed two dynamic modes in the high-molecular-weight solutions and quantitatively described their results using theory developed by Brochard and de Gennes.⁴⁶ According to the theory the two modes should correspond to two characteristic decay times: one being slow, τ_- ; and one being fast, τ_+ . The time-dependent intensity correlation function is then:

$$g(t) = 1 + [f_+ \exp(-\frac{t}{\tau_+}) + f_- \exp(-\frac{t}{\tau_-})]^2. \quad (4.3)$$

The decay times are given by:

$$\tau_{\pm}^{-1} = \frac{1 + q^2 \xi_{ve}^2 + \frac{\tau_{ve}}{\tau_q} \pm \sqrt{(1 + q^2 \xi_{ve}^2 + \frac{\tau_{ve}}{\tau_q})^2 - 4 \frac{\tau_{ve}}{\tau_q}}}{2\tau_{ve}}. \quad (4.4)$$

The amplitudes f_{\pm} are given by:⁴⁷

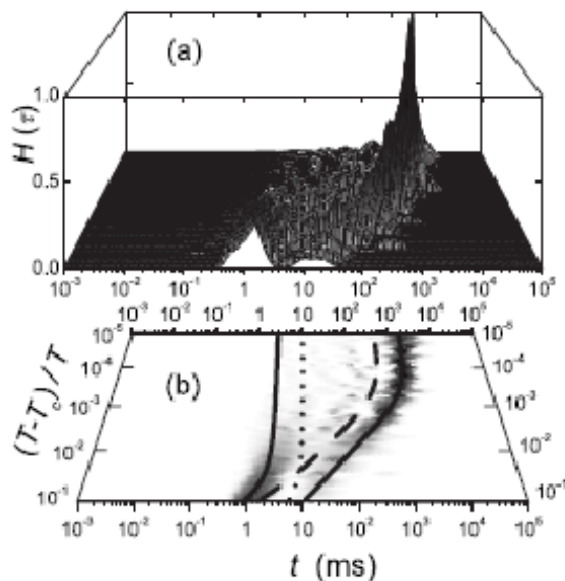


Figure 4.1: (a) A representation of the probability distribution analysis of the correlation function for the largest polymer sample observed with molecular weight $11.4 \times 10^{-6} \text{ g} \cdot \text{mol}^{-1}$ measured at $\theta = 30^\circ$ in the form of a 3-D graph. (b) gives the same graph as a grey-scale plot.⁴⁶

$$f_{\pm} = \pm \left[\frac{\tau_{ve}}{\tau_{\pm}} - (1 + q^2 \xi_{ve}^2) \right] \left(\frac{\tau_{ve}}{\tau_{+}} - \frac{\tau_{ve}}{\tau_{-}} \right)^{-1}. \quad (4.5)$$

The term τ_{ve} refers to the relaxation time of the viscoelastic mode which represents relaxation of polymer entanglements. The τ_q term is the diffusive relaxation time given by equation (4.1), ξ_{ve} is a viscoelastic length scale proportional to the radius of gyration. Interestingly, the lowest molecular-weight polystyrene sample showed only a single mode which corresponded to a correlation function that could be fitted to a single decay time of 5.2 ms.

For the higher molecular weight polymers, the two distinct modes were then fit to multiple theoretical calculations. It was found that the standard mode coupling

theory could not match the correlation functions of the higher molecular weight polymers and that a stretched exponential theory had to be employed. The stretched exponential is a simple modification of the form:⁴⁶

$$g(t) = 1 + [f_+ \exp(-\frac{t}{\tau_+})^{\beta_+} + f_- \exp(-\frac{t}{\tau_-})^{\beta_-}]^2, \quad (4.6)$$

where the stretching factors, β_{\pm} , have to be found by fitting the experimental data. The stretching factors broaden the coupled modes from the original theory and were found to fit the high probability regions from the probability distribution analysis very well.

4.2 Pre-transitional fluctuations of Liquid Crystals

Phase transformations in liquid crystals (LCs) differ greatly from those in ordinary fluids or polymers. Liquid crystals are a relatively new field of science and feature unique characteristics that would not be exhibited without their unusual molecular structure. While LCs have been seen for ages, their unique properties went unnoticed and undocumented until the 1880's.⁵² At this time many biological macromolecules were being studied while their LC properties went unnoticed. Friedrich Reinitzer was working with a cholesterol derivative when he realized that it passed from a clear to an opaque phase before solidifying as it cooled.⁵² This observation would eventually credit him with the discovery of LCs. Liquid crystals are primarily categorized by the phases they create, which are in turn categorized by the level of organization exhibited by that phase. In the isotropic phase a liquid

crystal exhibits complete disorganization. All molecules within the liquid are chaotically oriented. When cooled a liquid crystal may pass into a nematic phase. The nematic phase is more oriented as the molecules are all oriented generally along a director. Note that each molecule still maintains a certain level of chaotic orientation. In fact the amount that the molecules are oriented around the director can be quantified by the order parameter. The order parameter is calculated from the function $(3 \cos^2 \theta - 1)/2$ where the angle θ is the averaged angle of all molecules from the director.⁵³ In a nematic phase the direction of the director may change as one travels perpendicular to the director. This is called a chiral nematic liquid crystal phase, where the director rotates in one direction along director's perpendicular axis. The distance it takes for the director to make one full rotation is known as the pitch of the phase. This phase has some very useful optical properties which have been exploited for the creation of the liquid-crystal display (LCD). Note that a LC will have either a nematic phase or a chiral nematic phase, but not both.⁵³

As the LC is cooled it may also pass through a smectic phase which exhibits an even higher level of order. In the smectic phase the molecules are once again ordered along the director but are also positionally ordered in layers. If molecules in the layers are perpendicular to one another then it is a smectic A phase; if the molecules in the layers are oriented at some angle from one another one has a smectic C phase. There are new orientational patterns being discovered, and thus many other lettered smectic phases. A liquid crystal may, as it is cooled, exhibit more than one smectic phase of increasing order.⁵²

Two other major ways of categorizing LCs have been designated based on the

mechanism that causes the LC to form the ordered phase. The term *thermotropic* characterizes a LC that changes phase based on temperature. This term applied to pure liquid crystals such as the earlier example of cholesterol benzoate which exhibits a isotropic to chiral nematic transition at 178.5 C and a chiral nematic to solid transition at 145.5 C.⁵³ Other liquid crystals form organized structures only when dissolved in a particular solvent and have different behaviors based on the concentration in the solvent. These liquid crystals are called *lyotropic*. Only recently has a third characterization risen and become widely accepted. *Chromonic* LCs have recently become distinguished from what some call *discotic* or disk-shaped LCs. Chromonic LCs are distinct in that while LCs that fall into the previously discussed categories tend to be rod or cone shaped, chromonic LCs tend to be flat or planar.

The most common LCs are surfactants or lipids and have one end which is hydrophobic and one end which is hydrophilic and they tend to be flexible. This results in highly organized structures which actually decrease the overall entropy of the system. For chromonic LCs the rigid and inflexible plate like structures tend to stack into rods because the molecule will have a hydrophobic center surrounded by hydrophilic edges.⁵⁴ While non-chromonic LCs may tend to form micelles at a critical micelle concentration, chromonic liquid crystals have been shown to form rods in even dilute concentration. Some question still remains as to whether the length of the aggregates formed depends on temperature or concentration, but this particular property may be dependent on the molecule.⁵⁶ Chromonic LCs also do not exhibit a Krafft temperature where standard lyotropic LCs do. The Krafft

temperature is the temperature is the temperature below which the molecules will not self-organize.⁵⁶

4.3 Dynamic Light Scattering Study of Cromlyn Liquid Crystal Solution

As has been done with binary mixtures and polymer solutions, DLS has been used to conduct experiments to observe the pre-transitional fluctuations associated with the isotropic to nematic phase transition in a lyotropic chromonic liquid crystal. For this experiment we have chosen to use a chromonic liquid crystal called disodium cromoglycate (DSCG), also called *cromlyn*. Disodium cromoglycate is an excellent candidate for this study because much is known about the properties and behaviors of the molecule because it is used as a anti-asthmatic drug sold under the commercial name Intal. The IUPAC nomenclature for DSCG is disodium 5,5' - [(2-hydroxy-1,3-propanediyl)bis(oxy)] bis [4-oxy- 4H-1benzopyran-2-carboxylate]. A structural diagram for cromlyn can be seen in figure 4.2.

The pre-transitional fluctuations of DSCG were initially studied by Nastishin *et al.* in 2004.⁵⁴ However, at the time of that study only single photomultiplier tube photon counting systems were available to the research team, preventing cross-correlation of the signal, reducing the accuracy of the data, and inhibiting a complete understanding of the phenomena. Also measurements of the dynamics of the fluctuations were limited to five angles, 19, 45, 90, 109, and 135. In our new study, extensive measurements have been made including a total of eleven angles of depolarized (VV) light scattering measurements (where both the incident and measured light are vertically polarized) and seven angle of polarized (VH) light scattering mea-

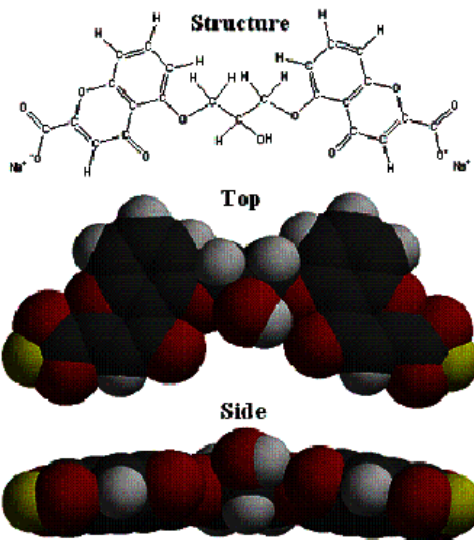


Figure 4.2: Structure diagram of Cromlyn⁵⁴

surements (where the incident and measured light are polarized 90° apart). This plethora of data will enable us to present a new and more accurate model to describe the pre-transitional fluctuations in chromonic liquid crystals.

Experiments on DSCG were conducted using the dynamic light-scattering setup utilizing two lasers and a dual photomultiplier photon counting system which is described in Chapter 1 of this thesis. The sample used was a 14% solution by mass of DSCG in deionized water. The DSCG was obtained from Spectrum Chemical Manufacturing Corp. in Gardena, CA. Prior to each experiment the sample was heated from the nematic phase to a minimum of 20°C above the transition temperature and allowed to sit at the elevated temperature for several days to ensure complete transition to the isotropic phase. The sample was then gently rotated about the horizontal axis to allow for complete mixing. An autocorrelation function was accumulated for each of the temperature steps for a minimum accumulation

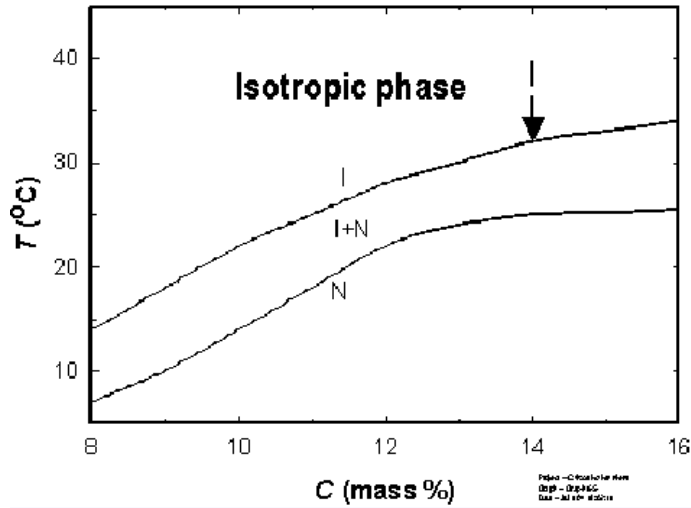


Figure 4.3: Phase diagram for lyotropic chromonic liquid crystal Cromlyn.⁵⁵

time of two hours. Temperature steps were chosen based on a logarithmic scale to provide more measurements and smaller steps close to transition temperature. Between temperature steps a minimum of 45 minutes was allotted for the sample to equilibrate at the next temperature. Depolarized light-scattering data were collected for angles of 15, 19, 30, 45, 60, 75, 90, 109, 120, 135, and 150 degrees. Polarized light-scattering data were collected for angles of 15, 30, 45, 75, 120, 135, and 150 degrees. The data were collected by using both ALV and Photocor software and analyzed by using both ALV and Dynals software. The resulting relaxation-time probability distributions for each temperature step were then plotted in contours to form a temperature-relaxation time contour plots, with the darker shades of orange representing higher probability associated with relaxation times. An example of one of these plots is shown in figure 4.4.

Nastishin *et al.* reported two dynamic modes: a diffusive mode consisting

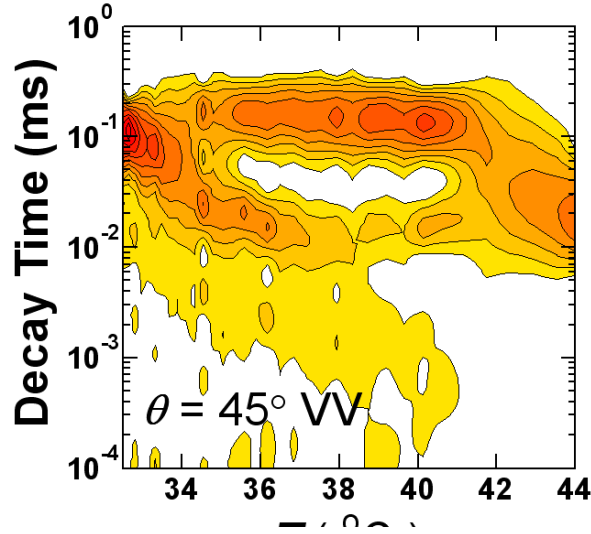


Figure 4.4: Example of a contour plot for the probability distribution of relaxation times versus temperature.

of fluctuations of concentration, and a relaxation mode consisting of fluctuations of anisotropy, apparently uncoupled. The diffusive mode did not show a pretransitional slowing down, whereas the orientational relaxation mode exhibited, as expected, a near-critical pretransitional slowing down. On the other hand, the diffusive mode can be tuned by the wave number, q , and can be made equally as slow as the relaxation mode at small q .

One of the fundamental problems in soft-matter physics is coupling between mesoscopic fluctuations which belong to different dynamic universality classes as was seen with polymers. The dynamics of pretransitional fluctuations in the isotropic phase of a lyotropic liquid crystal are complex. In addition to relaxations of the near-critical anisotropy fluctuations, one should expect relaxations of the fluctuations in concentration of the different particles present in the solution, including cromolyn aggregates, water molecules, and cromolyn monomers. The nematic order

parameter, the tensor of anisotropy, is "non-conserved". Thus, these fluctuations of anisotropy relax as relaxation dynamics with a characteristic relaxation time $\tau_R \sim \eta\chi$, where η is a "friction" (*e.g.*, viscosity) and χ is a "susceptibility". These three properties, τ_R , η , and χ , can be measured in cromolyn solution by dynamic light scattering, with a rheometer, and by static light scattering, as was done in Nastishin *et al.* Because it is non-conserved, the uncoupled relaxation time τ_R does not depend on the wave number q unless the susceptibility χ itself becomes q -dependent when the correlation length ξ becomes comparable with q^{-1} . This eventually happens close to the relevant second-order phase transition (the critical point) where the susceptibility as a function of the wave number can be represented by an Ornstein-Zernike approximation:⁵⁹

$$\chi \simeq \frac{\chi_0}{1 + \xi^2 q^2}, \quad (4.7)$$

where χ_0 , the susceptibility in the "thermodynamic limit", can be obtained by extrapolating the light-scattering intensity to zero q , and ξ is the correlation length.

Contrarily, the concentration is a "conserved" order parameter. Uncoupled concentration fluctuations relax according to the diffusion dynamics with an explicitly q -dependent relaxation time following equation (4.1). Note that D may itself may become q -dependent if the correlation length of the concentration fluctuations is comparable with q^{-1} .⁶⁰ A coupling between the modes, belonging to different dynamic universality classes, may change this picture. Therefore, to detect such a coupling, one needs to accurately determine q -dependencies of "effective" (ob-

servable) dynamic modes. Such was the case for the polymer solutions previously described.

The first new results to be discussed are those from the static-light scattering data. The intensity of light scattering as a function of temperature in the isotropic phase of cromolyn solution for the VV alignment is shown in figure 4.5. The open circles indicate experimental data for the inverse intensity. Close to the transition, the intensity is proportional to the pretransitional nematic susceptibility χ , which, according to the Landau-de Gennes theory, diverges at the temperature of the absolute stability limit of the isotropic phase T^* .⁶⁰

$$\chi_o = \frac{l_o^3}{k_B (T - T^*)}, \quad (4.8)$$

where k_B is Boltzman's constant and l_o is a characteristic length of the anisotropic molecules or aggregates. The dashed line shows the Landau-de Gennes law for the inverse susceptibility (the measure of the pretransitional nematic fluctuations) near the nematic-isotropic transition. The VV intensity contains contributions from both isotropic and anisotropic light-scattering.

The data points in figure 4.5 clearly show crossover from weak, largely isotropic, light scattering above 50°C, to overwhelming anisotropic light-scattering proportional to the Landau-de Gennes susceptibility below 35°C. The middle of this range, T_A , corresponds to the inflection point in the temperature dependence of the inverse intensity, and may be designated as the "onset" of cromolyn aggregation. The relatively sharp transition from the weak molecular scattering to strong anisotropic

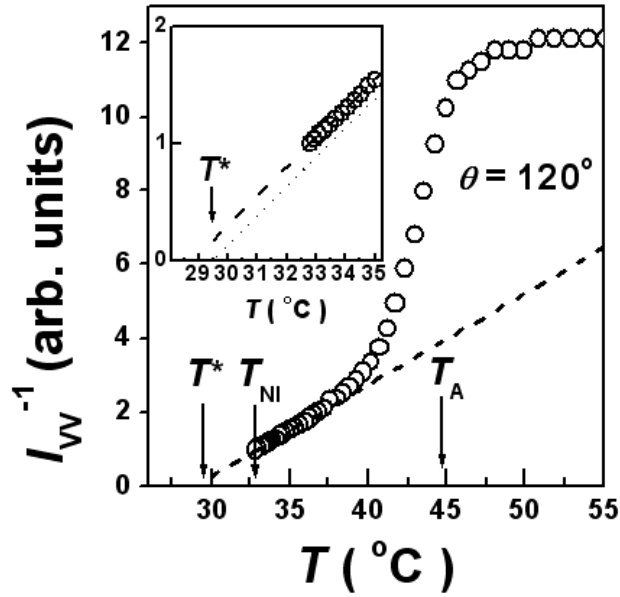


Figure 4.5: Inverse intensity of vertically polarized light scattering at scattering angle $\theta = 120^\circ$ as a function of temperature. Open circles represent experimental data. Dashed line shows the linear approximation, valid below 35°C . Dotted line represents the Landau-de Gennes behavior for the nematic susceptibility χ_o^{-1} given by equation (4.8) and magnified in the inset. The dotted line is shifted down from the dashed line by a constant proportional to $\xi_o^2 q^2$. The temperature $T^* \simeq 30^\circ\text{C}$ is the absolute limit of the isotropic phase, $T_A \simeq 45^\circ\text{C}$ indicates the onset of cromolyn aggregation.

scattering that is associated with the existence of supramolecular aggregates favors an interpretation of the cromolyn aggregation similar to micellization of amphiphilic molecules. In the case of micelles, once the micellization temperature is crossed, the number of micelles increases at expense of the number of monomers, while the average size of the micelles (average aggregation number) remains stable.⁷⁶ The static light scattering data shown in 4.5 cannot alone answer the question of whether the cromolyn aggregates continue to grow with cooling, or if their concentration increases while the average size remains the same. Thus we compare the static light scattering data with the viscosity data, which shows that the viscosity of the cromolyn aqueous solution has an anomalous growth upon cooling to the transition temperature T_{NI} .⁵⁴ Such an anomaly does not usually exist in the isotropic phase of thermotropic nematics and, therefore, Nastishin *et al.* attributed it to elongation of supramolecular aggregates (rods) of cromolyn molecules when the temperature decreases.⁵⁴ This anomaly of the viscosity could also be attributed to an increase in the aggregate concentration upon cooling. Without further information this viscosity anomaly cannot be fully explained.

The correlation length:

$$\xi \simeq \xi_0 \left[\frac{(T - T^*)}{T} \right]^{-\frac{1}{2}} \propto \chi_0^{\frac{1}{2}}, \quad (4.9)$$

of the pretransitional nematic fluctuations was obtained from the q -dependence of the intensity of static light scattering by Nastishin *et al.*⁵⁴ The amplitude of the correlation length (an effective range of orientational interactions), $\xi_0 \simeq 2 \text{ nm}$,⁵⁴

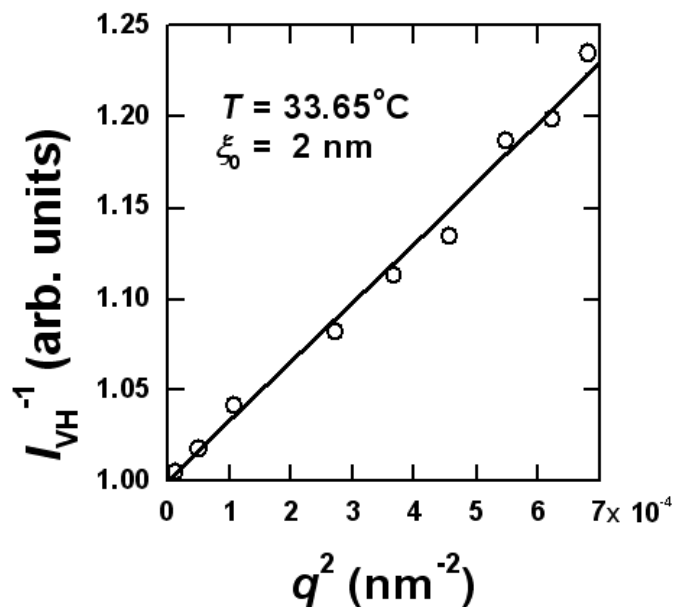


Figure 4.6: An Ornstein-Zerike plot of the inverse intensity of the anisotropic scattering in the isotropic phase of cromolyn solution at 33.65°C as a function of the wave number obtained with the alternative setup and use of immersion.

is close to the diameter of cromolyn aggregates,⁵⁸ being about three times smaller than the length of the aggregates. The correlation length was confirmed by new measurements made on an alternative DLS setup which utilizes a decaline immersion cell to minimize stray light and increase the accuracy of the measurements. Figure 4.6 shows the results of these measurements and demonstrates that the pre-transitional susceptibility indeed follows the Ornstein-Zernike approximation given equation (4.7).

Analyses of orientational and translational dynamics of anisotropic scatterers are complicated, especially for the VV alignment where both isotropic and anisotropic scattering are present.^{61, 62, 63, 64, 65} In particular, for the VV alignment it is practically impossible to extract the decay times by direct approximation of

the correlation function to multi-exponentials, thus creating the need to represent data using decay time probability distributions. These plots for all VV angles are presented in Appendix A.

For all eleven scattering angles studied with the VV alignment, we have observed two or three of the pronounced "ridges" in the probability distributions of decay time plots. These ridges, however, only reveal to us observable modes which are merely a combination of actual modes when coupling and masking effects are at play in the system. Masking effects, for the purpose of this study, will be defined as the effect resulting when the strong scattering from one dynamic mode prevents the weaker scattering from a second dynamic mode from clearly appearing in the decay time probability distribution analysis. For example, at large angles the positions of the probability maxima do not depend much on the proximity to the transition, but do strongly depend on the wave number, and thus might be interpreted as associated with two diffusion modes (see Appendix A $\theta = 150^\circ$). In contrast, at small angles the apparent fast mode becomes strongly temperature dependent exhibiting a slowing down near the transition to the nematic phase and thus might be attributed to relaxation of anisotropy fluctuations (see Appendix A, $\theta = 15^\circ$). This leaves the question: What happens with the fast diffusion mode at small q and with the relaxation mode at large q ?

The information needed to answer this question can largely be drawn from the results for the VH alignment of light scattering. The value of cross-polarization measurements is that no isotropic scattering is present. The three-dimensional probability distributions of decay times obtained for the VH alignment for all angles are

presented in Appendix B. In this alignment, within the experiment resolution, we have reliably observed a single dynamic mode, which we attribute to relaxation of anisotropic fluctuations. Figure 4.7 shows dynamic autocorrelation functions, acquired from the cromolyn solution with both the PhotoCor-FC correlator and ALV-5000/E correlator for the VH alignment at two scattering angles, 15° and 150° for selected temperatures. The time-dependent intensity autocorrelation functions $g_2(t)$ were fitted to stretched exponentials as

$$g_2(t) - 1 = A \exp\left(-\frac{t}{\tau}\right)^\beta, \quad (4.10)$$

where τ is a characteristic decay time, A is an amplitude, and β is a stretched-exponential parameter that characterizes the width of the decay-time distribution.

The parameter β , shown in figure 4.8, varies from 0.5 far from the transition to 0.6 close to the transition; these values are similar to reported for high-molecular-weight polymer solutions.⁴⁶ The average decay times, defined as

$$\langle\tau\rangle = \frac{\tau}{\beta} \Gamma\left(\frac{1}{\beta}\right), \quad (4.11)$$

where $\Gamma(1/\beta)$ is the probability distribution function, appear to be very close to the positions of the maxima of the probability distributions, especially close to the transitions.

In figure 4.9 the contour maps show equal probability distributions of decay times. The open circles show maxima of the probability distributions. The crosses indicate average decay times obtained from the fits of the correlation functions to

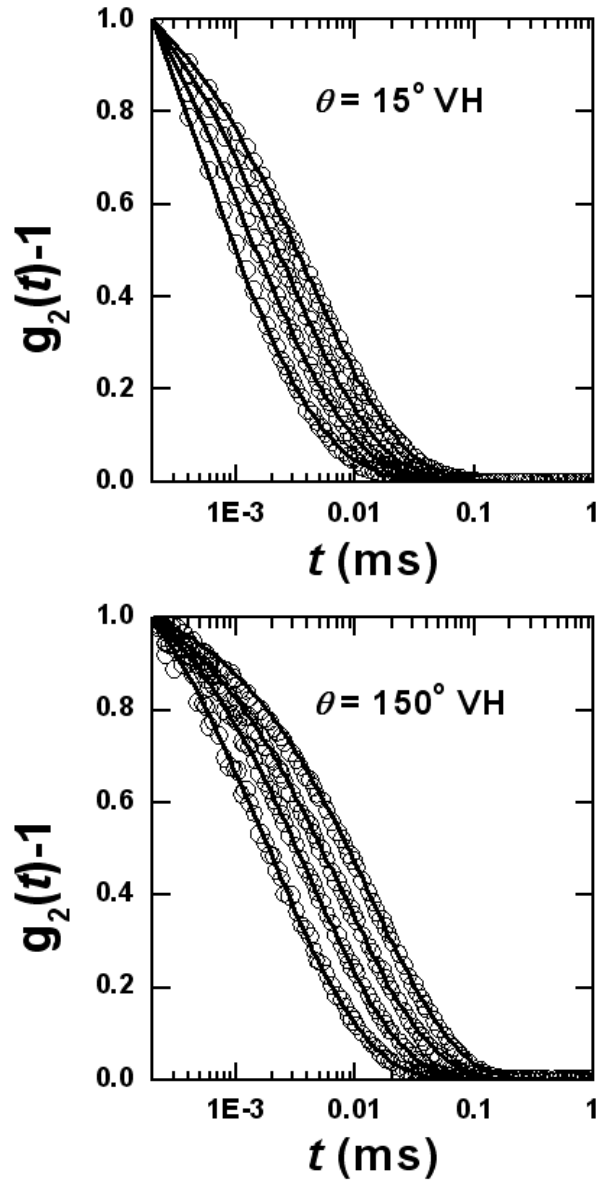


Figure 4.7: Examples of the dynamic auto-correlation functions at $\theta = 15^\circ$ (a) and $\theta = 150^\circ$ (b) obtained with the ALV correlator (a) and the PhotoCor correlator (b). The PhotoCor correlator allows obtaining the correlation function at $t < 5 \cdot 10^{-3}$ ms.

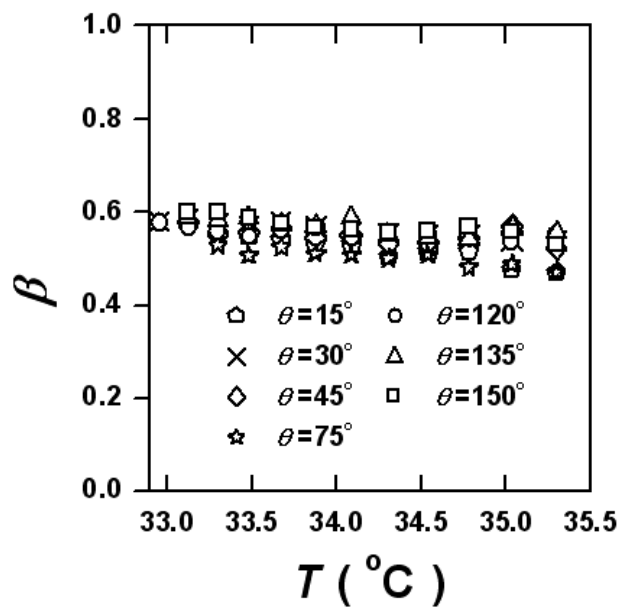


Figure 4.8: Stretched exponential parameter as a function of temperature.

stretched exponentials from equation (4.10).

Average decay (relaxation) times of anisotropic fluctuations, $\langle\tau\rangle_{\text{VH}}$, in the isotropic phase of cromolyn solution obtained at different angles as a function of temperature are shown in figure 4.10. While for all scattering angles $\langle\tau\rangle_{\text{VH}}$ strongly depends on the proximity to the phase transition, it also significantly depends on the light scattering wave number, suggesting a coupling between orientational dynamics and diffusion-like dynamics.

Average decay rates of anisotropic fluctuations in the isotropic phase of cromolyn solution as a function of the light-scattering wave number for different selected temperatures are shown in figure 4.11a. Here the decay rate ($\Gamma = \tau^{-1}$) is used rather than the decay time for a clearer presentation of the data. The various symbols indicate the temperatures ranging from 36°C to 32.8°C . It is immediately seen from

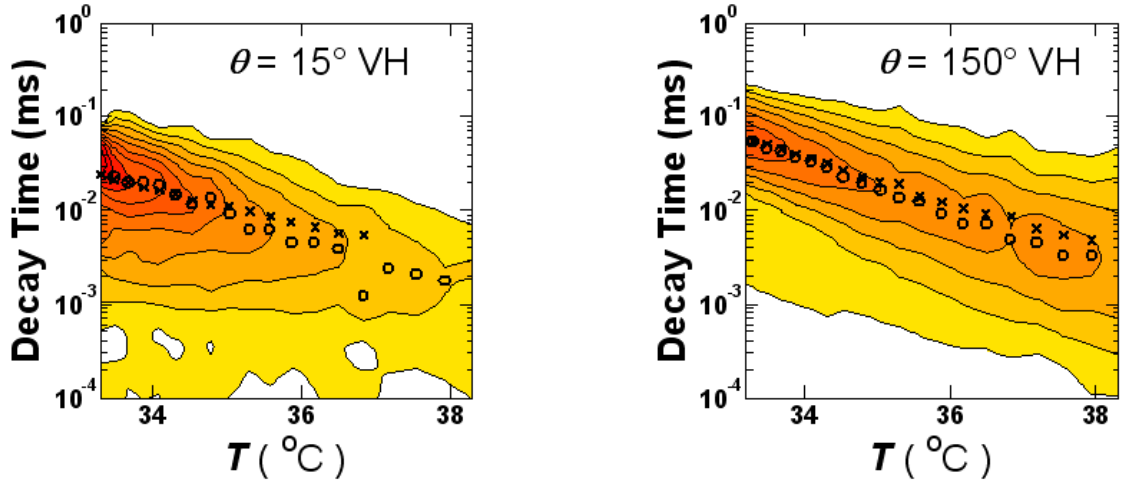


Figure 4.9: Decay times for the VH alignment of light scattering in the isotropic phase of cromolyn solution at $\theta = 15^{\circ}$ (a) and $\theta = 150^{\circ}$ (b). The contour maps show equal probability distributions of decay times. The open circles show maxima of the probability distributions. The crosses indicate average decay times obtained from the fits of the correlation functions to stretched exponentials given by Eq. (4.10).

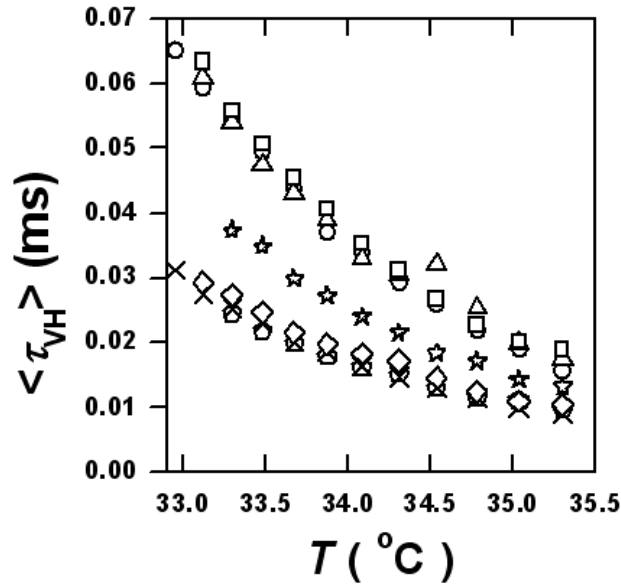


Figure 4.10: Average ("effective") decay times of the anisotropic fluctuations in the isotropic phase of cromolyn solution as a function of temperature. The symbols indicate different scattering angles as in figure 4.8.

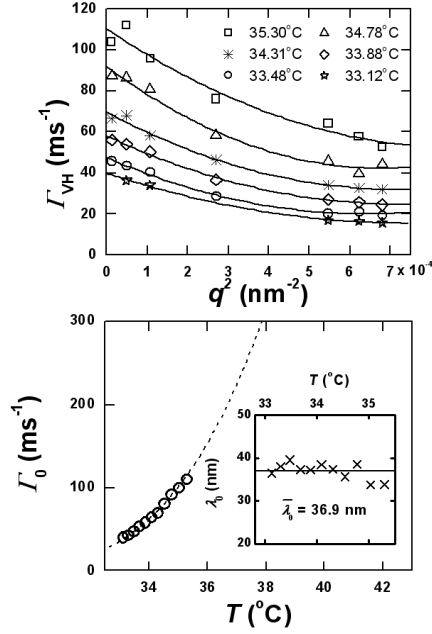


Figure 4.11: Top: Average decay rates of anisotropic fluctuations in the isotropic phase of cromolyn solution as a function of the light-scattering wave number for different selected temperatures. Symbols indicate various temperatures. Solid lines are q^2 -linear approximations as given by Eq. (4.12). The data for 32.7°C were collected only for two angles: $\theta = 19^\circ$ and $\theta = 105^\circ$. Bottom: Uncoupled decay rates of fluctuations of anisotropy, τ_0 , as a function of temperature. The open circles are the values obtained by extrapolation of $\tau_{VH}(q)$ to $q = 0$. The dashed curve is fit to Eq. (4.13). The coupling length is shown in inset as a function of temperature (crosses) with a solid line denoting the average.

figure 4.11 that there is an unusual q -dependence of the anisotropic relaxation rate. As previously discussed, there should be a minimal variation of the relaxation rate with the wave-number, q , and $\langle\Gamma_{\text{vH}}\rangle$ should exhibit a slight increase when q is large, not when q is small as shown. This q -dependence was so unusual that independent measurements were made to confirm the phenomenon on a second DLS instrument which was tested for error due to heterodyning and found to be in excellent working order. The results of this measurement are presented in figure 4.12. The results confirm that the unusual behavior of the relaxation rate is not an artifact of experimental error. Within the resolution of our experiment, the data in figure 4.11a can be approximated by:

$$\langle\Gamma_{\text{vH}}\rangle = \Gamma_{\circ} (1 - \Lambda_1^2 q^2 + \Lambda_2^4 q^4), \quad (4.12)$$

where Γ_{\circ} is the average relaxation rate extrapolated to $q = 0$, and is attributed to "uncoupled" anisotropic fluctuations; and $\Lambda_{1,2}$ are characteristic lengths which play the role of a coupling constant for relaxation and diffusion. The uncoupled relaxation rate of fluctuations of anisotropy (Γ_{\circ}) as a function of temperature is shown in Fig. 4.11b. The temperature dependence of Γ_{\circ} is in good agreement with the prediction for the dynamics of the pretransitional fluctuations of anisotropy in liquid crystals⁶⁰:

$$\Gamma_{\circ} = \frac{1}{\chi\eta} \simeq \frac{k_{\text{B}}(T - T^*)}{l^3\eta}, \quad (4.13)$$

where χ is the pretransitional nematic susceptibility given by equation (4.8) and

$T^* = 29.5^\circ \text{ C}$ obtained from the static light-scattering. The viscosity data were taken from Nastishin *et al.*⁵⁴ The only adjustable parameter is the length $l \simeq 5.5$ nm, which may be interpreted as the average length of cromolyn aggregates. Taking into account that the intermolecular distance along the aggregate axis is $\delta \simeq 0.34$ nm,^{56, 57} one can conclude that the aggregation number in the temperature range $36\text{-}33^\circ\text{C}$ is about 16 monomer units.

The coupling parameters $\Lambda_{1,2}$ from equation (4.12) are characteristic lengths of the system. They determine the wave-number (length scale) at which the average decay rate finds a minimum value. The minimum value is:

$$q_o = \sqrt{\frac{\Lambda_1^2}{2\Lambda_2^4}}, \quad (4.14)$$

where $\lambda_o \equiv 1/q_o$.

At this point we have given as much description to the depolarized light scattering data as is currently possible. From here on the polarized scattering data will be discussed. The polarized scattering data are a very complex mixture of anisotropic scattering and diffusive scattering which is seen only in observable modes as opposed to either pure anisotropic or pure diffusion modes. By using the data from the VH study, it is possible to better understand this complicated picture and hopefully decipher the observable modes found in the VV data. Figure 4.13 shows the apparent decay times for the VV alignment of light scattering in the isotropic phase of cromolyn solution for $\theta = 15^\circ, 30^\circ, 45^\circ,$ and 150° .

The dashed curve in each panel indicate the relaxation times, $\langle\tau_{\text{VH}}\rangle$, of the

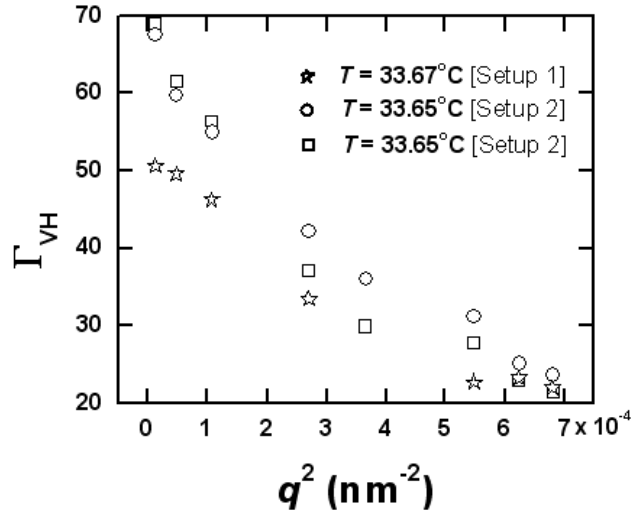


Figure 4.12: The q –dependence of the anisotropic fluctuations is shown using two different DLS equipment setups. Data from the original instrument are represented by stars while data from a second instrument have been analyzed by two separate methods represented by circles and squares.

coupled anisotropic fluctuations in accordance with equation (4.12). One can see from these projections that the peaks of the ridges do not follow the relaxation dynamics of anisotropic fluctuations at small q , but the peaks of the ridges do seem to follow the dashed curve at large q . Unlike the near-critical dynamics of anisotropic fluctuations from the VH data, the positions of the apparent slow mode (seen best along the top straight lines in figure 4.13) and of the apparent fast mode (seen best along the bottom straight lines in figure 4.13) do not strongly depend on the proximity to the transition temperature but do strongly depend on the wave number. This is why we interpret the apparent slow mode as a slow diffusion and the apparent fast mode as a fast diffusion associated with relaxation of isotropic fluctuations of concentration of cromolyn aggregates and monomers, respectively.

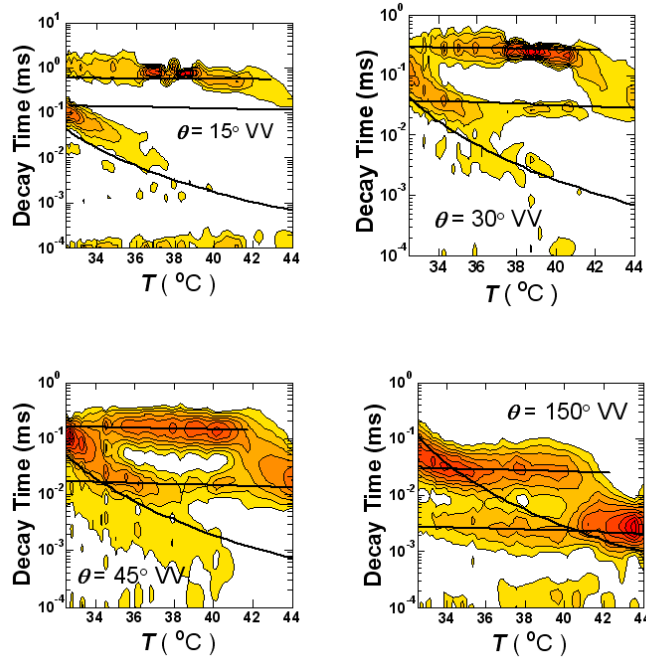


Figure 4.13: Decay times for the VV alignment of light scattering in the isotropic phase of cromolyn solution at $\theta = 15^\circ$ (a), $\theta = 30^\circ$ (b), $\theta = 45^\circ$ (c), and $\theta = 150^\circ$ (d). The contour maps show equal probability distributions of decay times. The two almost parallel lines indicate two uncoupled diffusion modes as predicted by Eq. (4.16) from the data obtained at about 39°C . The solid curve represents the behavior of the effective relaxation time of the anisotropy fluctuations obtained from the VH light scattering alignment, as given by Eq. (4.12).

The diffusion coefficients for these two modes were obtained as slopes of q^2 linear plots (seen in figure 4.14) in the range of temperatures where these modes are most likely uncoupled from the "hidden" relaxation mode of anisotropic fluctuations:

$$\frac{1}{\tau_{D_{1,2}}} = D_{1,2}q^2, \quad (4.15)$$

where $D_{1,2}$ are the diffusion coefficients for the slow mode (D_1) and fast mode (D_2) respectively. Each presumably uncoupled diffusion mode was approximated with a Stokes-Einstein expression as

$$D_1 \simeq \frac{k_B T}{6\pi\eta_s R_1}, \quad (4.16)$$

$$D_2 \simeq \frac{k_B T}{6\pi\eta_s R_2}, \quad (4.17)$$

where η_s is the viscosity of the solvent (water), $R_1 \simeq l \simeq 5.5$ nm and $R_2 \simeq 0.5$ nm. Based on the values obtained for R_1 and R_2 , we attribute these diffusion modes to the diffusion of the cromolyn aggregates and monomers, respectively. These two diffusion modes are shown as two parallel solid lines in figure 4.13. With all three lines plotted, it is apparent that the positions of the probability maxima do not always correspond to the actual dynamic modes. The positions of the maxima of the apparent fast mode seen in figure 4.13a become strongly temperature dependent below 36°C, and are, in fact, superpositions of two modes: relaxation (dashed curve), and fast diffusion (lower dashed line). The positions of the maxima of the apparent slow mode seen in figure 4.13b below 35°C are also superpositions of two modes:

relaxation (dashed curve) and slow diffusion (upper dashed line). Enhancements of the two diffusion times as a function of temperature close to the transition indicate that the approximations given by equations (4.16) and (4.17) may fail very close to the transition, either due to some temperature dependence of R_1 and R_2 or because the viscosity of solvent does not exactly represent the effective viscosity.

This description of the diffusion modes still leaves the observed orientation mode unexplained. At temperatures close to the aggregation temperature (T_A), we have identified two diffusion modes with the two observed ridges in the decay time distribution. In this temperature range, the locations of these ridges are strongly q -dependent and weakly temperature dependent as would be expected of diffusion modes. However, at temperatures very close to the transition, the two observed ridges have different characters. One ridge becomes weakly q -dependent and strongly temperature dependent, while the other remains strongly q -dependent and weakly temperature dependent. This signals the presence of a mode with stronger scattering intensity. We attribute this new behavior to the emergence of an orientational mode, resulting from the relaxation of fluctuations in cromolyn aggregate orientation, which grows in strength (scattering intensity) on approaching the isotropic-nematic phase change critical temperature, T_{NI} . Just as we saw in both static light scattering and depolarized dynamic scattering, we see that the intensity of anisotropic fluctuations increases strongly as the transition temperature is approached.

We have characterized the VH anisotropic fluctuations in the previous section and found a strongly temperature dependent and q -dependent mode. However, we

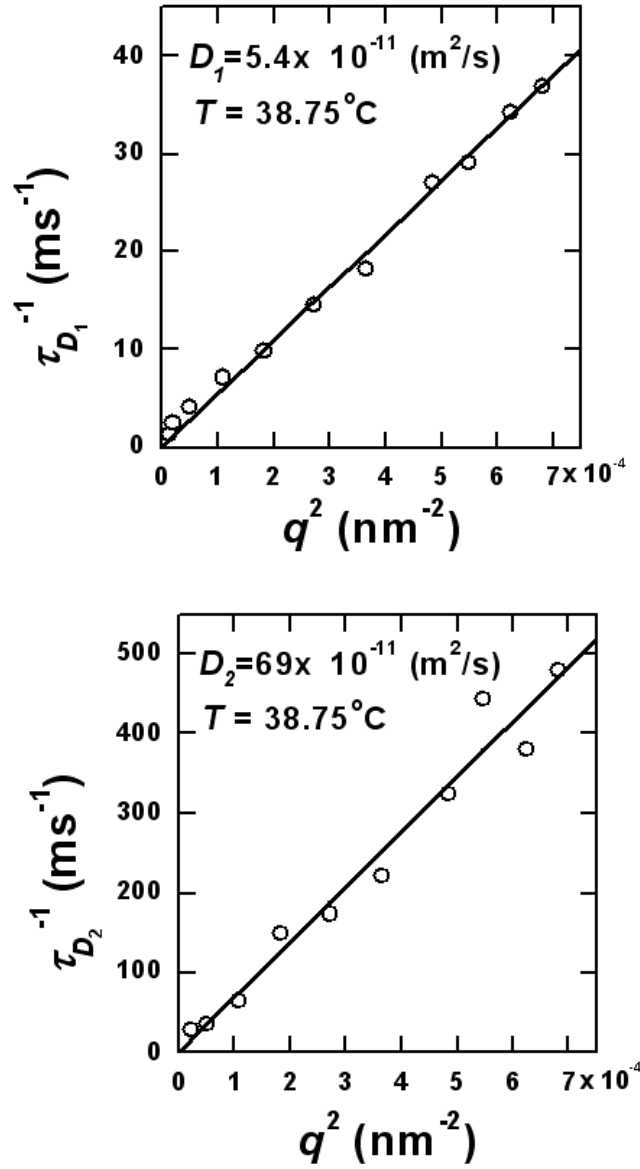


Figure 4.14: Wave-number dependence of the inverse diffusion times of the isotropic fluctuations at selected temperatures: for slow diffusion (top) and for fast diffusion (bottom). Symbols show the experimental data, solid straight lines indicate the approximations given by Eq. (4.15).

do not expect that the dynamic mode associated with the VV anisotropic fluctuations will share the same wave-number dependence as the VH mode, because the components of the anisotropy tensor connected to each of these geometries have different symmetry properties, which constrain possible dynamic couplings.⁶⁰ Indeed, it is seen in figure 4.13 that the ridges of the anisotropic fluctuations do not show the same q -dependence as the VH anisotropic fluctuations represented by the dashed curves. Instead, only at $\theta = 150^\circ$ does the line representing the anisotropic fluctuations overlay the peaks of the temperature dependent ridge. The dynamic mode visible in VV is actually that portion of the anisotropic tensor that corresponds to the minimum value of the relaxation rate from equation (4.12) so that:

$$\Gamma_{\text{VV}} = \Gamma_{\text{VH}}(q_0). \quad (4.18)$$

It can be seen in figure 4.11a that this minimum corresponds to a q value close to 150° , explaining why only at that angle do the peaks of the temperature dependent ridges follow the dashed curve representing equation (4.12).

The two diffusion modes seen at higher temperatures should not physically disappear from the dynamics as the temperature of the system is lowered. Instead, it is most likely that the resolution of the data-analysis procedure becomes less sensitive to the existence of these modes as the orientational mode grows in strength (scattering intensity). We have already seen evidence that the diffusion mode associated with cromolyn aggregates was weak enough to become effectively invisible to the data analysis procedure at small scattering angles (i.e. $\theta = 15^\circ$). Therefore, it

is reasonable to suspect that the cromolyn monomer diffusion mode becomes overwhelmed by the orientational mode. For large wave numbers when the decay time of the orientational mode and the slow diffusion mode are comparable, the slow diffusion mode also appears to be overwhelmed by the stronger scattering of the orientational mode. This second effect, due to the analysis, is manifested at $\theta = 150^\circ$ as the slow mode taking on a value intermediate to the expected orientation and slow diffusion values, and at $\theta = 15^\circ$ by the "disappearance" of the slow diffusion mode at temperatures where the decay times appear to cross those of the orientational mode. This is the reason why the fast mode, seen in the VV alignment at $\theta = 30^\circ$ was attributed to the relaxation of the pretransitional anisotropy fluctuations by Nastishin *et al.*⁵⁴

In summary, a very unusual phenomenon of pretransitional fluctuation dynamics has been observed. The pretransitional fluctuations in liquid crystals cannot be described by the equations found from pure and binary fluids, or those used in polymer solutions. While static light scattering data agreed with previously published data on cromolyn, enhancements in scattering techniques have allowed for observing dynamic correlation features never seen before, including the strange q -dependence of the anisotropic scattering. This wave-number dependence is so unusual in fact, that an independent experiment was conducted with a second DLS instrument to confirm the existence of the effect. The significant decrease of the effective relaxation rate of the anisotropy fluctuations with increase of the light scattering wave number q is unusual because all conventional models for coupling between the relaxation dynamics of a non-conserved order parameter (such as the

tensor of anisotropy) and diffusion (q -dependent) relaxation of a conserved order parameter (such as concentration) predict an opposite effect. This is likely due to rare properties of chromonic liquid crystals which exhibit a strong increase in shear viscosity prior to the isotropic to nematic phase change. It is still unclear whether the change in viscosity is a result of the elongation of rods or due to an increased concentration of the rods. It was also found that by using the VH alignment to observe the anisotropic scattering, it was possible to better understand the data obtained from the VV alignment. The combination of static, polarized dynamic, and depolarized dynamic light scattering allowed for the calculation of the correlation length, stretching parameters, relaxation times, and diffusion coefficients. However, thus far only a brief qualitative explanation of this plethora of data is available. The above discussion serves only to provide some insight into the unusual nature of the data, but does not give a theory to describe the phenomena as an appropriate theory of pretransitional fluctuations has yet to be found for the observed behavior in lyotropic liquid crystals. Future work is being done to develop a new theory to describe fluctuations in chromolyn.

CHAPTER 5

CONCLUSIONS

This thesis describes a focused study of applying dynamic light scattering to three of the most popular topics in contemporary chemical and biomolecular engineering problems: polymers, proteins, and liquid crystals. These studies have demonstrated capabilities and limitations of dynamic light scattering, as well as highlighting future applications and advancements to be made in the field. When measuring polymer samples of PEG, it was found that DLS is capable of making size measurements of nanometer-size particles in solutions. The limitations of DLS were also demonstrated in that DLS requires very clean samples free of dust and isolated aggregates. This limitation was in part overcome by new software that will, in the future, greatly improve the abilities of DLS to make more accurate measurements in more complicated systems. In this polymer study comparison of size measuring techniques was also seen. It was found that often in literature the size of a nano-scale particle is reported either as a hydrodynamic radius (R_h), or as a radius of gyration (R_g) depending on the instrument used to measure the particles. Little research has been made to compare the two sizes, and more research needs to be done to clarify the differences between the two.

Research on the protein GroEL showed how DLS can be used to monitor the kinetics of protein aggregation. By combining the statics and dynamics of the system, it was possible to compare the aggregation of GroEL to the aggregation of other proteins even when no visible precipitant was formed. Such observation

could in theory determine whether a certain type of aggregation is reversible as well whether the process is diffusion-limited or rate-limited. These are important questions to be answered as the field of biomolecular engineering continues to tackle the problems of protein folding and aggregation and the forces that drive them.

Finally, in studying cromolyn, DLS was used to observe the very complex physics of the pretransitional fluctuations of a rare type of liquid crystal. The lyotropic chromonic liquid crystal cromolyn exhibits an unusual wave-number dependence of the anisotropic scattering. This q -dependence of the anisotropic scattering had gone previously unnoticed in earlier studies, but due to improvements in measuring and analytical techniques, DLS was able to find this new phenomena. While the physics of the observed pretransitional fluctuations has only been described, and not fully explained, this study still very much shows the unique capability of light scattering to be able to observe fluctuations.

It is very clear from these experiments that DLS has not yet reached its full potential as a scientific instrument. As new fields of scientific research and engineering move out of the micro-scale realm and into the realm of nano- and meso-scale, fluctuations will become more and more important. While many methods exist for measuring small particles, DLS remains the primary method for directly measuring fluctuations. Improvements in computer software and hardware along with improvements to laser technology make DLS an ever more powerful tool. To this end it is easy to see how the dynamic light scattering instrument will be the new microscope to the "nano-generation".

CHAPTER 6

APPENDIX A: CONTOUR PLOTS FROM DEPOLARIZED SCATTERING

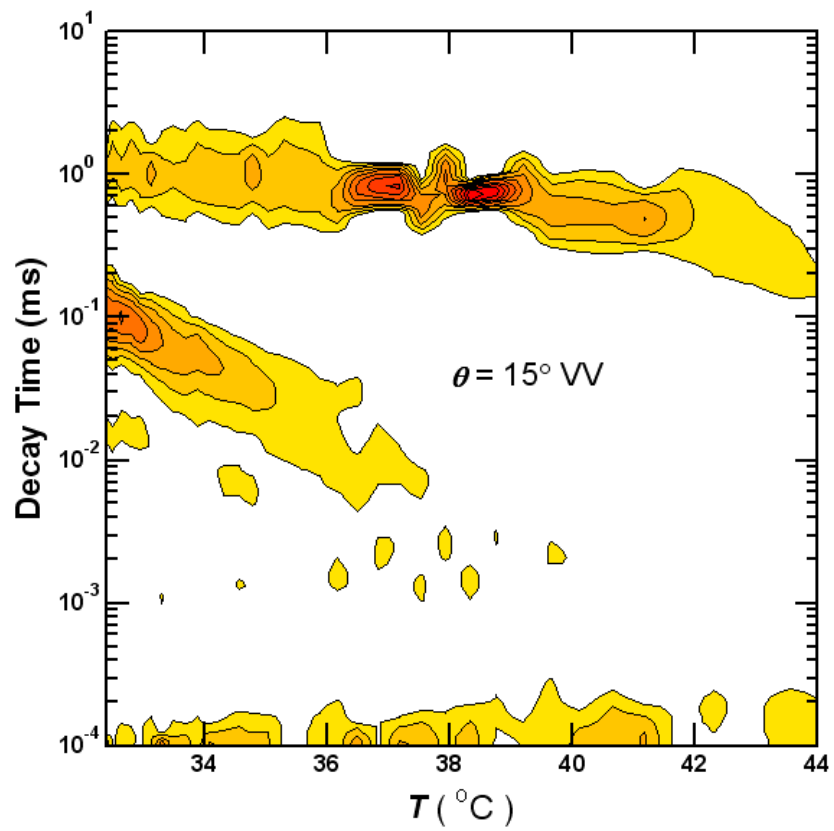


Figure 6.1: Contour plot for 15°scattering angle and VV alignment. Darker color contour areas represent higher probability for the relaxation time.

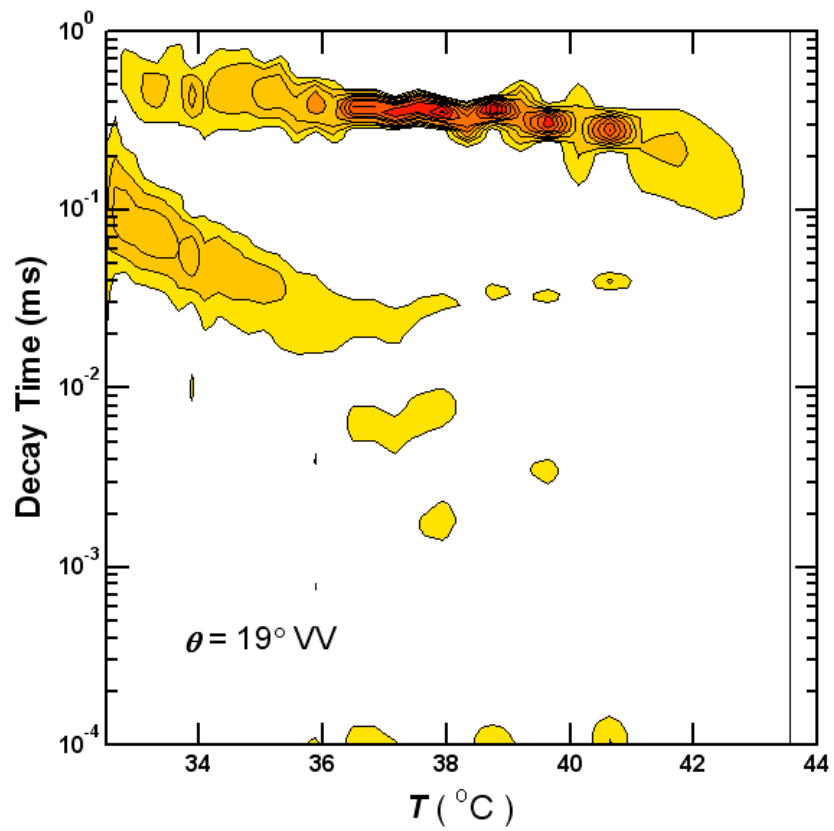


Figure 6.2: Contour plot for 19° scattering angle and VV alignment. Darker color contour areas represent higher probability for the relaxation time.

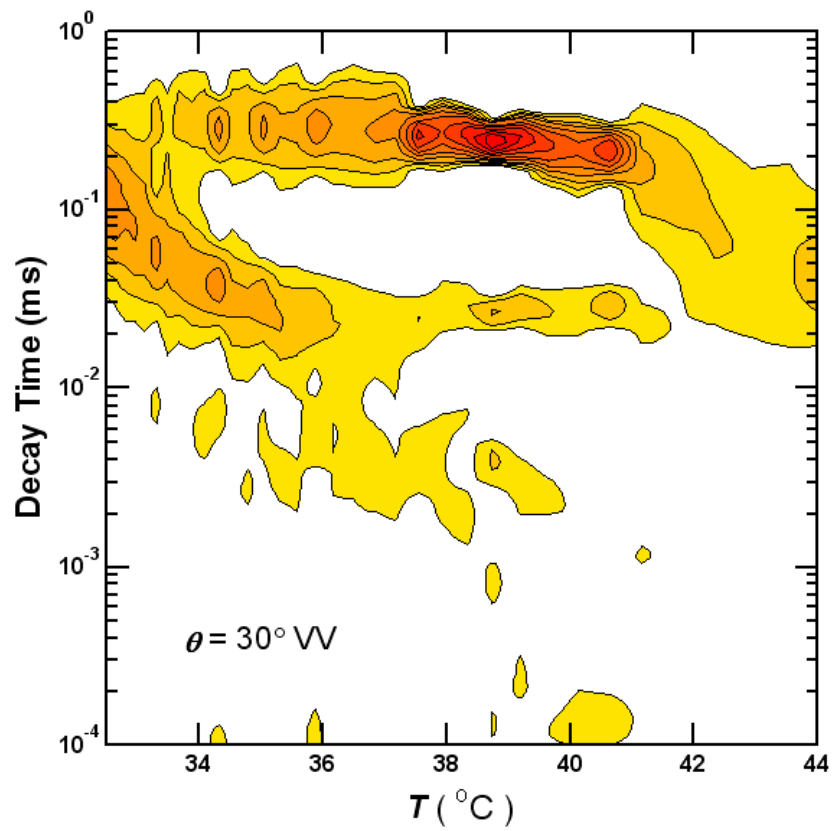


Figure 6.3: Contour plot for 30° scattering angle and VV alignment. Darker color contour areas represent higher probability for the relaxation time.

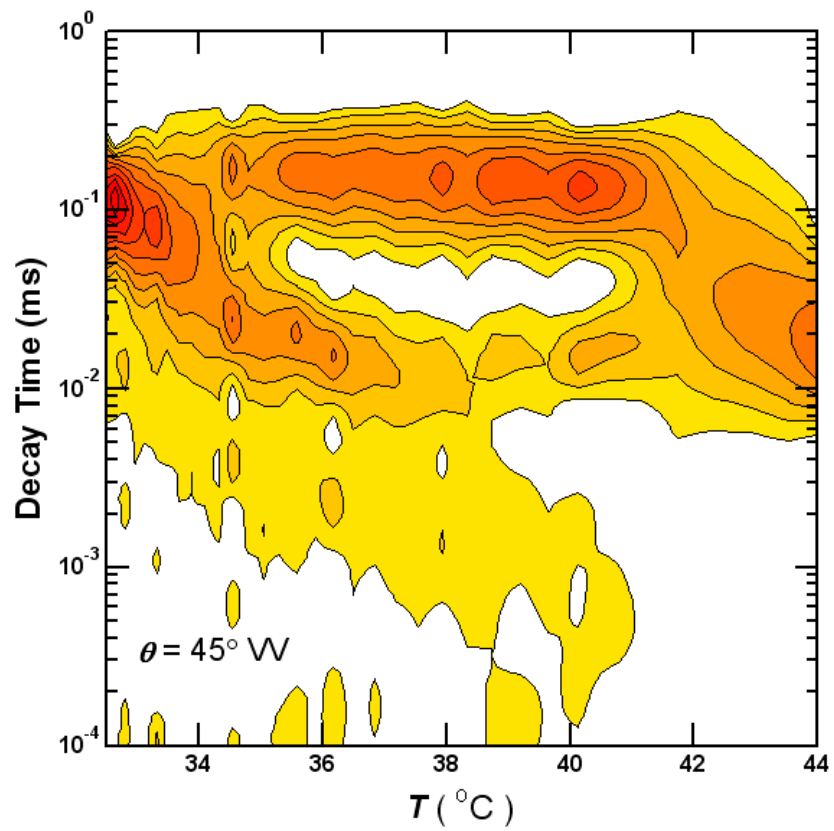


Figure 6.4: Contour plot for 45° scattering angle and VV alignment. Darker color contour areas represent higher probability for the relaxation time.

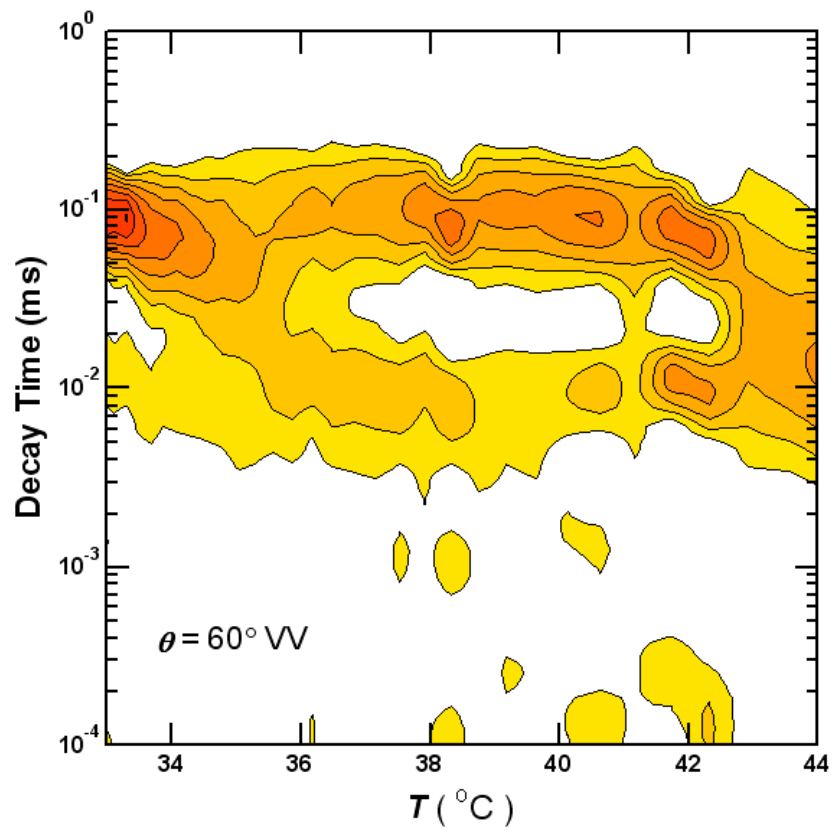


Figure 6.5: Contour plot for 60° scattering angle and VV alignment. Darker color contour areas represent higher probability for the relaxation time.

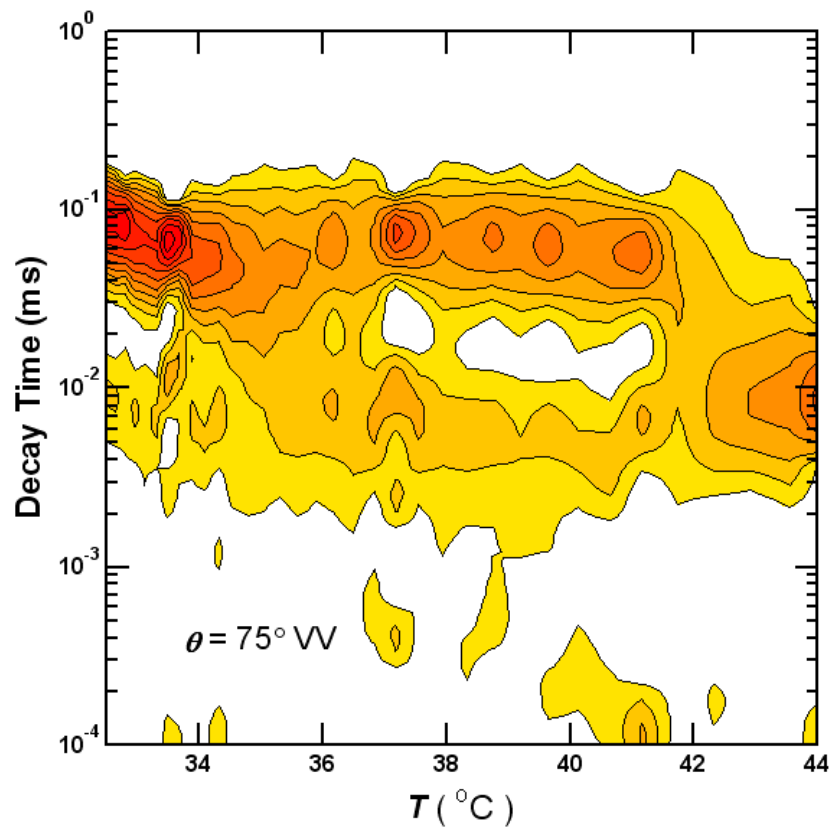


Figure 6.6: Contour plot for 75° scattering angle and VV alignment. Darker color contour areas represent higher probability for the relaxation time.

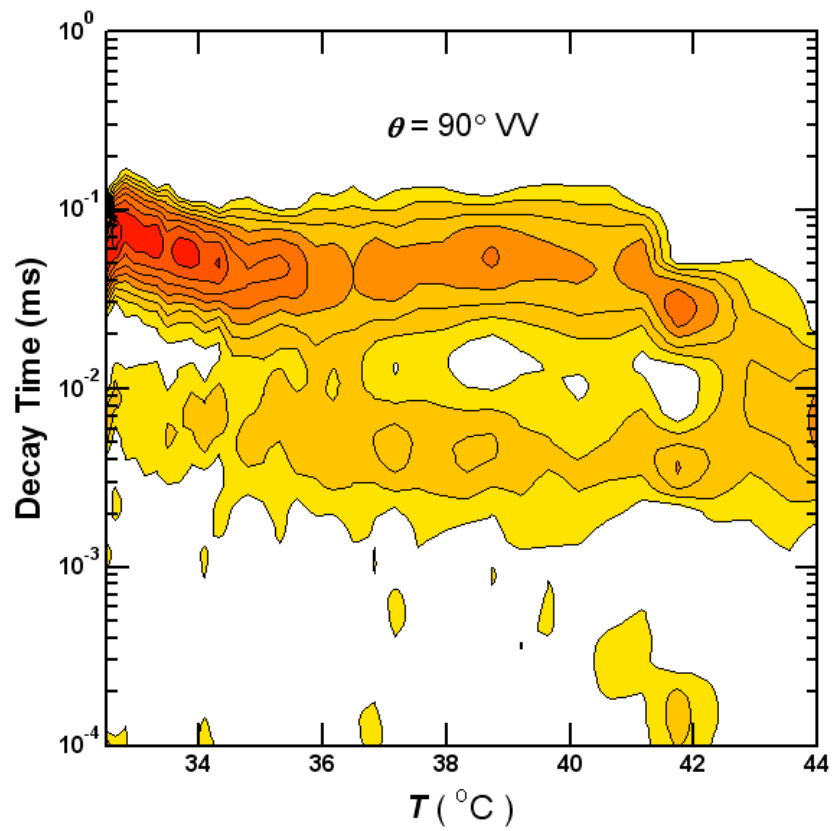


Figure 6.7: Contour plot for 90° scattering angle and VV alignment. Darker color contour areas represent higher probability for the relaxation time.

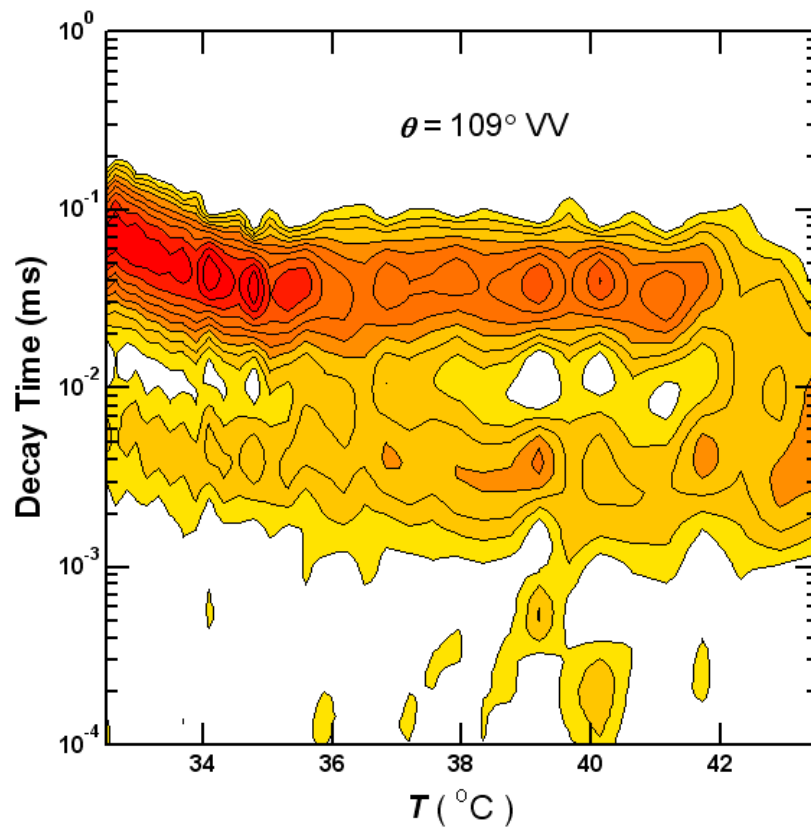


Figure 6.8: Contour plot for 109° scattering angle and VV alignment. Darker color contour areas represent higher probability for the relaxation time.

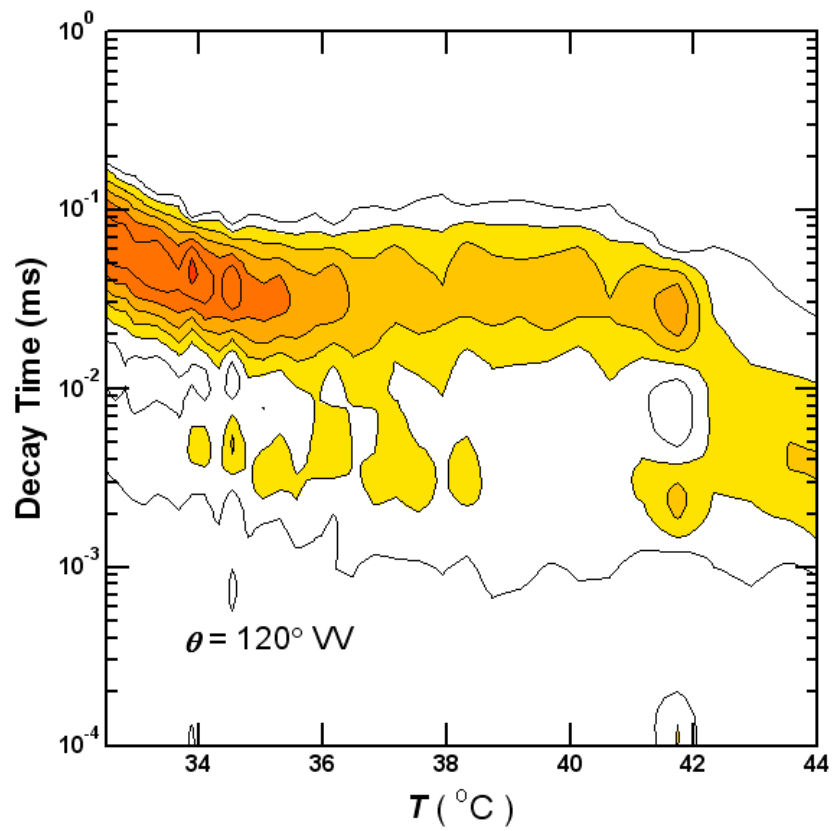


Figure 6.9: Contour plot for 120° scattering angle and VV alignment. Darker color contour areas represent higher probability for the relaxation time.

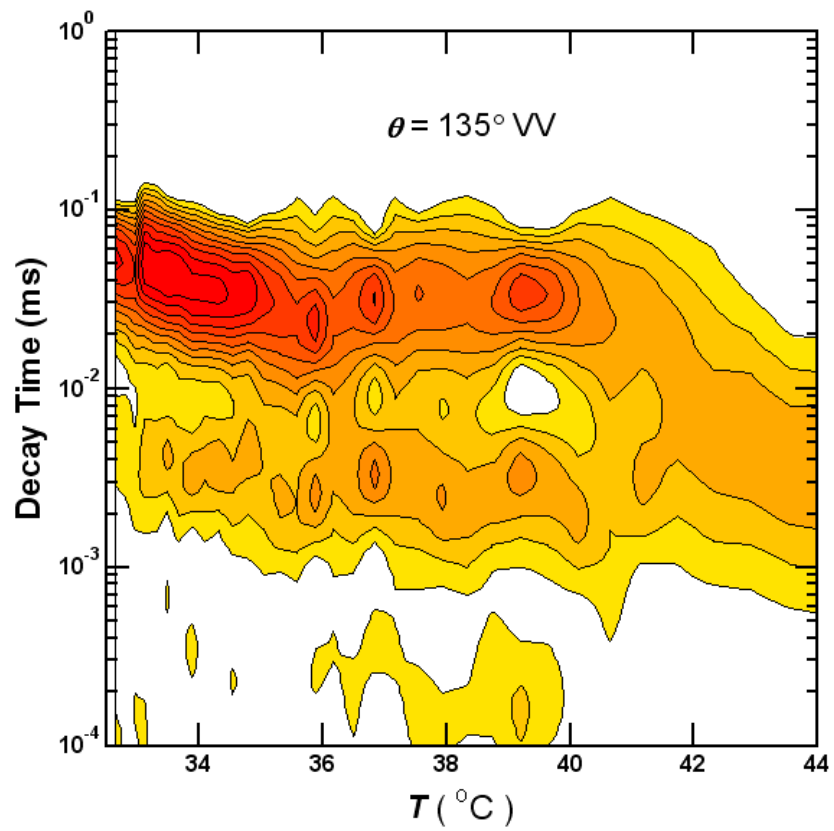


Figure 6.10: Contour plot for 135° scattering angle and VV alignment. Darker color contour areas represent higher probability for the relaxation time.

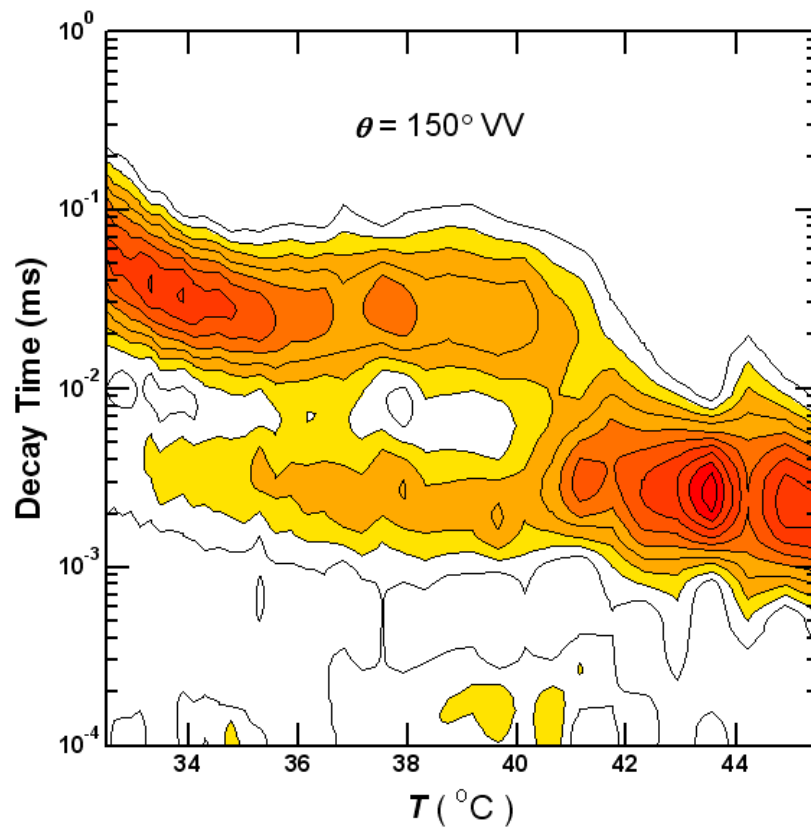


Figure 6.11: Contour plot for 150° scattering angle and VV alignment. Darker color contour areas represent higher probability for the relaxation time.

CHAPTER 7

APPENDIX B: CONTOUR PLOT FROM POLARIZED LIGHT

SCATTERING

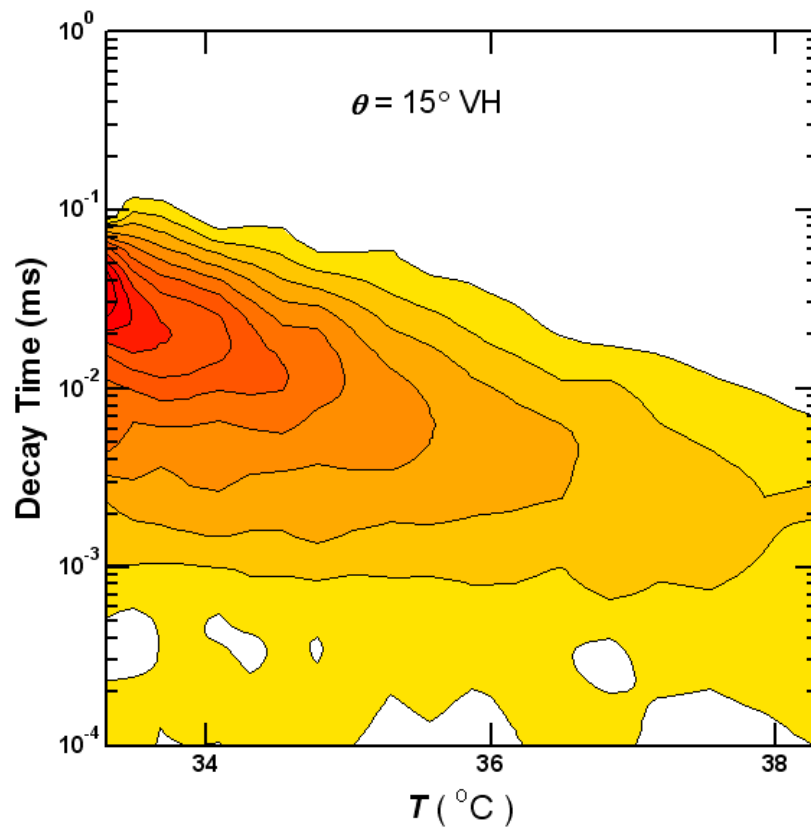


Figure 7.1: Contour plot for 15° scattering angle and VH alignment. Darker color contour areas represent higher probability for the relaxation time.

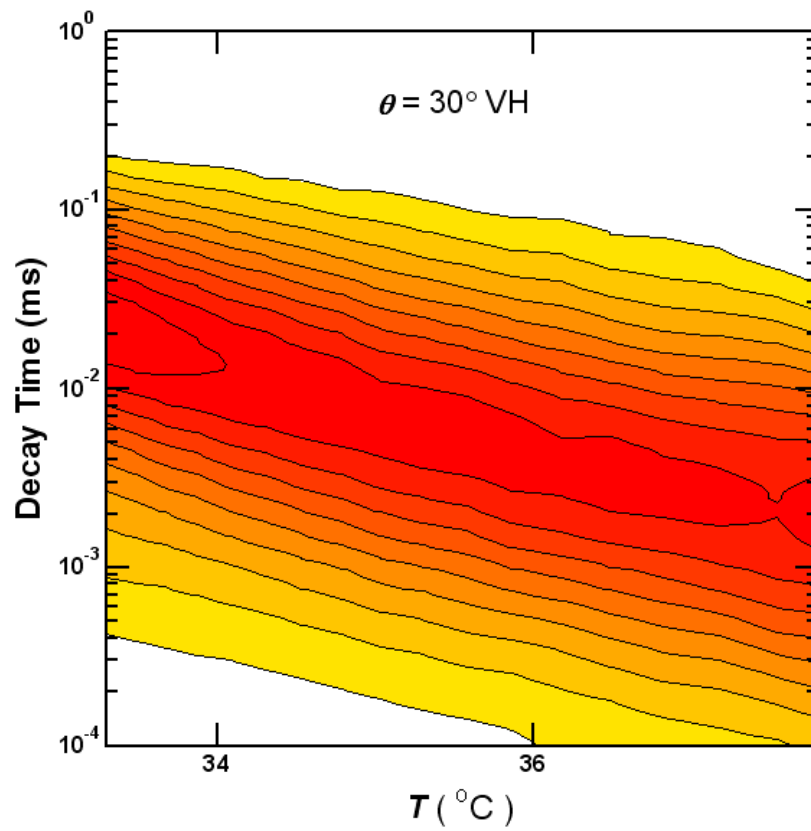


Figure 7.2: Contour plot for 30° scattering angle and VH alignment. Darker color contour areas represent higher probability for the relaxation time.

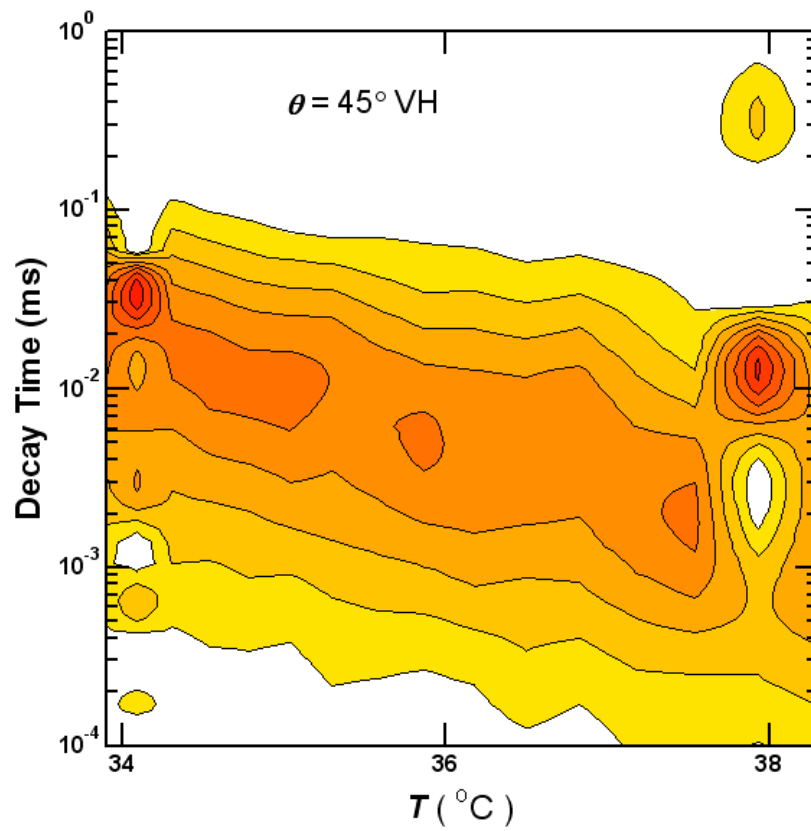


Figure 7.3: Contour plot for 45° scattering angle and VH alignment. Darker color contour areas represent higher probability for the relaxation time.

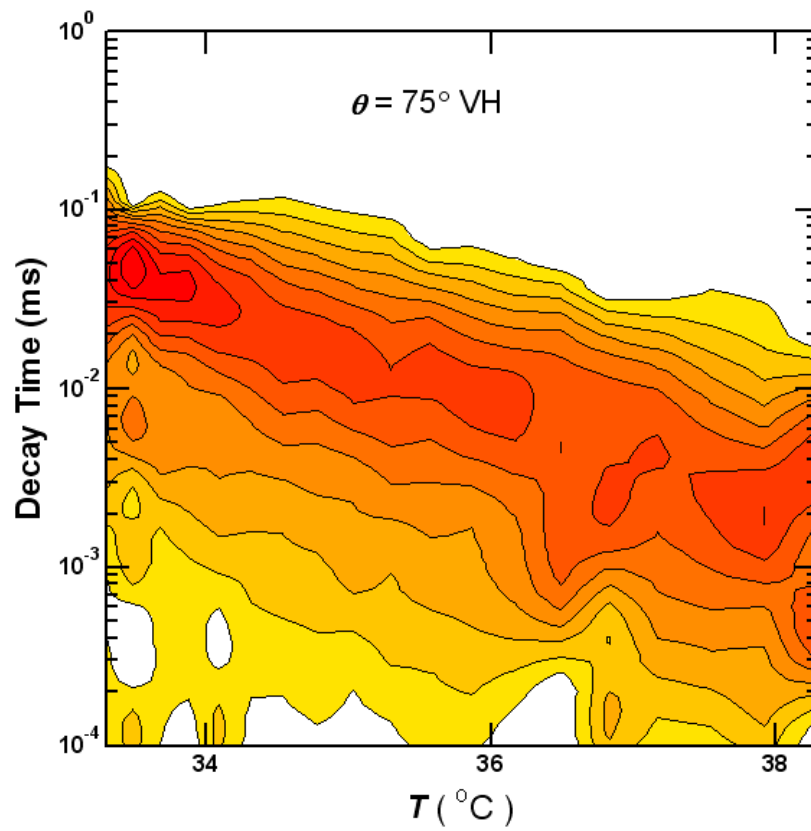


Figure 7.4: Contour plot for 75° scattering angle and VH alignment. Darker color contour areas represent higher probability for the relaxation time.

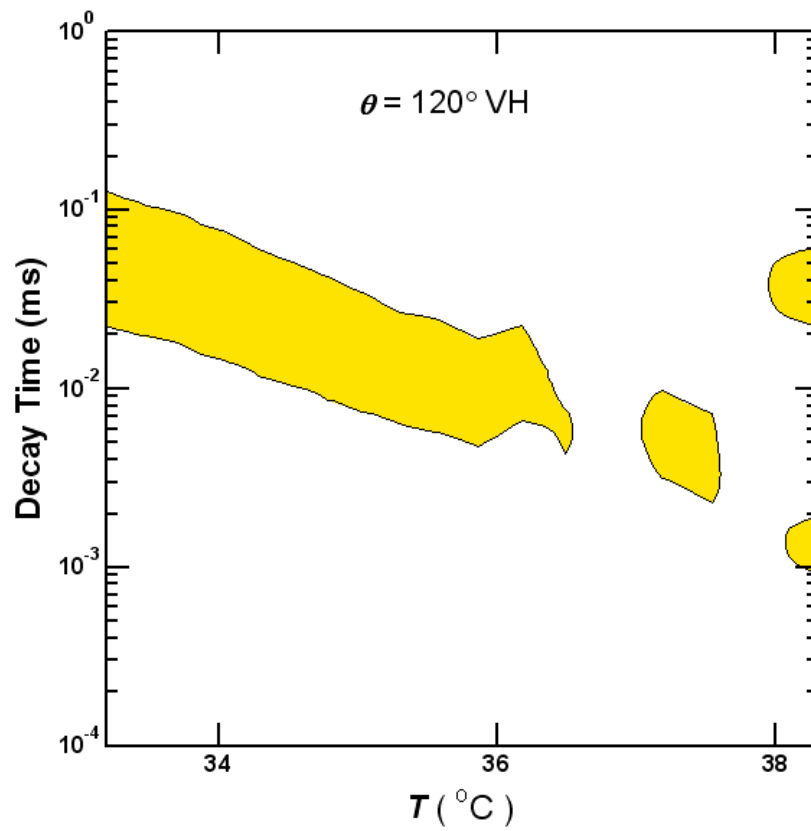


Figure 7.5: Contour plot for 120° scattering angle and VH alignment. Darker color contour areas represent higher probability for the relaxation time.

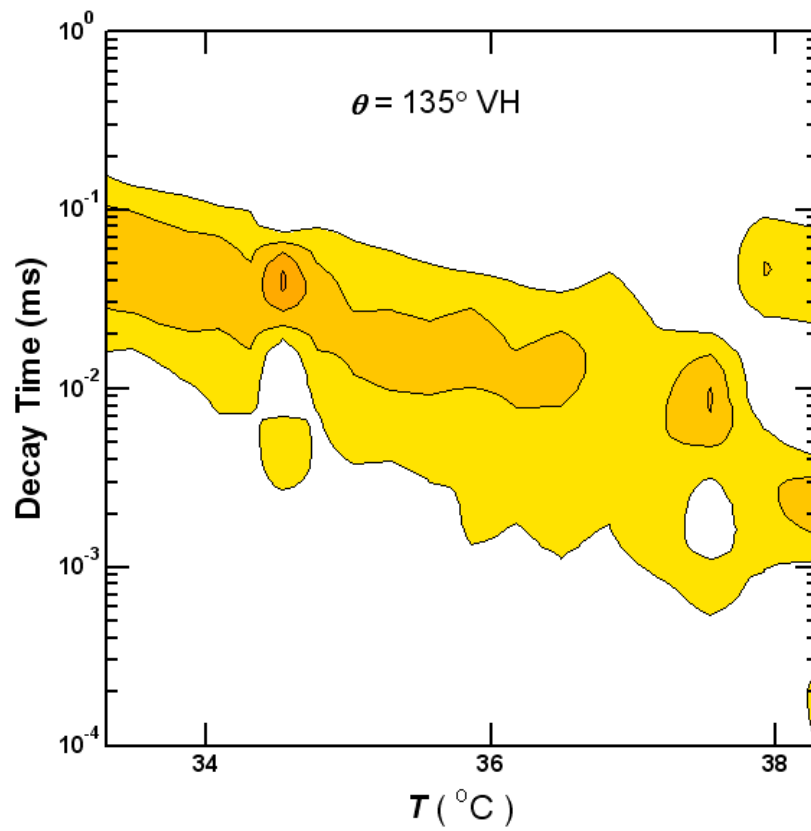


Figure 7.6: Contour plot for 135° scattering angle and VH alignment. Darker color contour areas represent higher probability for the relaxation time.

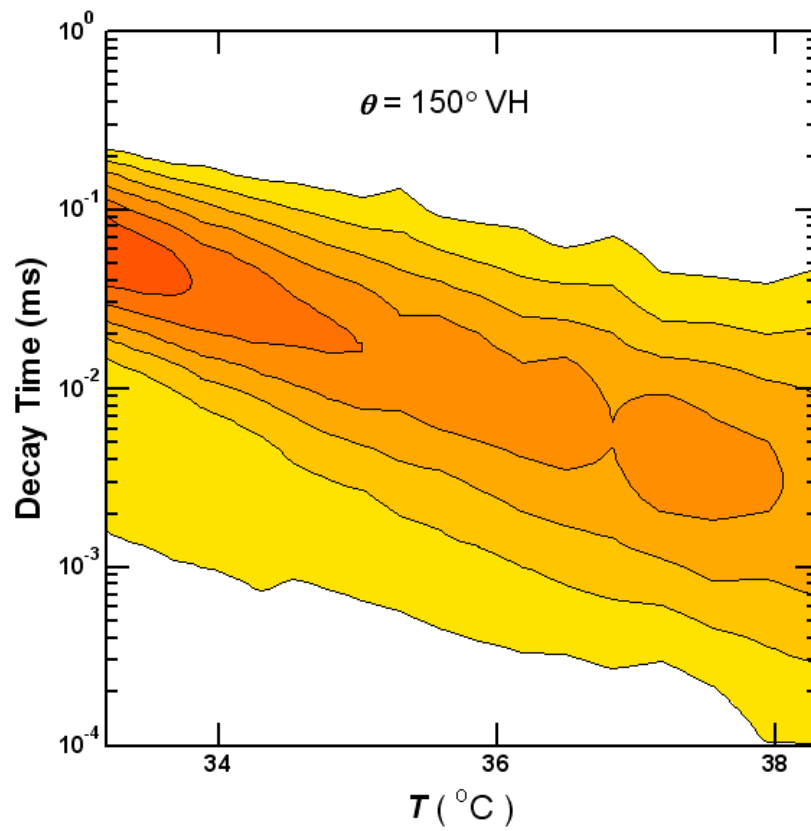


Figure 7.7: Contour plot for 150° scattering angle and VH alignment. Darker color contour areas represent higher probability for the relaxation time.

REFERENCES

1. B. J. Berne and R. Pecora, *Dynamic Light Scattering with applications to chemistry, biochemistry and physics* (Dover Publications, Mineola, 2000).
2. *Dynamic Light Scattering: Applications of Photon Correlation Spectroscopy* edited by Robert Pecora (Plenum Press, New York, 1985).
3. H.N.V. Temperley, J.S. Rowlinson, and G.S. Rushbrooke, *Physics of Simple Liquids* (North-Holland Publishing Company, Amsterdam, 1968).
4. I. L. Fablinskii, *Molecular Scattering of Light* (Plenum Press, New York, 1968).
5. E.Gross, Z. Phys **63**, 685 (1930).
6. A. Einstein, Ann. Physik **33**, 1275 (1910).
7. A.M. Evtyushevkov, Y.F. Kiyachenko, Olefirenko, and I.K. Yudin, Instruments and Experimental Techniques **24**, 1265 (1981).
8. M.A. Anisimov, A.M. Evtyushenkov, Y.F. Kiyachenko, I.K. Yudin, JETP Letters **20**, 170 (1974).
9. Y.F. Kiyachenko and I.K. Yudin, Instruments and Experimental Techniques **21**, 1082 (1978).

10. I.K. Yudin, G.L. Nikolaenko, V.I. Kosov, V.A. Agayan, M. A. Anisimov, and J.V. Sengers, *Intl. J. of Thermophys.* **18**, 1237 (1997).
11. H.C. Van de Hulst, *Light Scattering by Small Particles* (Dover Publications, New York, 1981).
12. T.C. Rich, D. A. Pinnov, *Applied Optics* **13**, 1376 (1974).
13. R.A.L. Jones, *Soft Condensed Matter* (Oxford University Press, New York, 2002).
14. M.L. Alessi, A. Norman, S. Knowlton, D. Ho, and S. Greer, *Macromolecules* **38**, 9333 (2005).
15. R. Shresth, R. McDonald, and S. Greer, *J. Chem. Phys.* **117**, 9037 (2002).
16. A.Toumi, M. Bouanz, A. Gharbi, *Chem Phys. Lett.* **362**, 567 (2002).
17. A. Norman, B. Manvilla, E. Frank, J. Niamke, G. D. Smith, S. Greer, *Macromolecules* (2008).
18. A. Norman, Y. Fei, D. Ho, S. Greer, *Macromolecules* **40**, 2559, (2007).
19. N. Ouerfelli, M. Bouanz, *J. Solution Chem.* **35**, 7 (2006).
20. K. Devanand, J.C. Selser, *Macromolecules.* **24**, 5943 (1991)
21. R. C. Weast and M. J. Astle, in *CRC Handbook of Chemistry and Physics* 60th ed. (CRC Press, Boca Raton,1980).
22. Lewis, and Macdonald, *J. Amer. Chem. Soc.* **55**, 3057 (1933)

23. B. Hammouda, D. Ho, S. Kline, *Macromolecules* **35**, 8578 (2002)
24. A. Faraone, S. Magazu, G. Mazano, P. Migliardo, E. Tattamanti, V. Villari, J. Chem. Phys. **110**, 1801 (1999).
25. Y. Panyukov, I. K. Yudin, V. Drachev, E. Dobrov, and B. Kurganov, *Biophysical Chem.* **127** (2007)
26. Y. Panyukov, M. Nemykh, E. Rafikova, B. Kurganov, L. Yaguzhinsky, A. Arutyunyan, V. Drachev, and E. Dobrov, *Int. J. Biochem. Cell Biol.* **38**, 533 (2006).
27. V. Militello, C. Casarino, A. Emanuele, A. Giostra, F. Pullara, and M. Leone, *Biophysical Chem.* **107**, 175 (2004).
28. J. Schüler, J. Frank, W. Saenger, and Y. Georgalis, *Biophys. J.* **77**, 1117 (1999).
29. F. A. Bettelheim, R. Ansari, Q. F. Cheng, and J. S. Zigler Jr., *Biochem. and Biophys Res. Comm.* **261**, 292 (1999).
30. H. Khanova, K. Markossian, B. Kurganov, A. Samoilov, S. Kleimenov, D. Levitsky, I. Yudin, A. Timofeeva, K. Muranov, and M. Ostrovsky, *Biochemistry* **44**, 15480 (2005).
31. M. A. Speed, J. King, D. I. C. Wang, *Biotechnology and Bioengineering*, **54**, 333 (1997).
32. J. King, C. Haase-Pettingell, A. S. Robinson, M. A. Speed, and A. Matraki, *The FASEB Journal* **10**, 33 (1996).

33. J. W. Chen and D. L. Smith, *Biochemistry*, **39**, 4250, (2000).
34. K. Braig, and Z. Otwinowski, *Nature* **371**, 6498 (1994).
35. K. Braig, P. D. Adams, and A. T. Brunger, *Nature Structural Biology* **2**,1083 (1995).
36. "GroEL/GroES Complex", Computing Research Academy, www.cra.org (2007).
37. N. C. Price, S. M. Kelly, G. J. Thomson, J. R. Coggins, S. Wood, and A. A. D Mauer, *Biochemica ET Biophysica ACTA* **1161**, 52 (1993).
38. T. Mizobata, and Y. Kawata, *Biochemica Et Biophysica Acta - Protien Structure and Molecular Enzymology* **1209**, 83 (1994).
39. J. J. Gilijamse, A. J. Lock, and H. J. Bakker, *Proc. Natl. Acad. Sci. USA* **102**, 3202 (2005).
40. P. Thiyagarajan, S. J. Henderson, and A. Joachimiak, *Structure* **4**, 79 (1996).
41. Y. Igarashi, K. Kimura, K. Ichimura, S. Matsuzaki, T. Ikura, K. Kawajima, H. Kihara, *Biophys. Chem.* **53**, 259 (1995).
42. M. Arai, T. Inobe, K. Maki, T. Ikura, H. Kihara, Y. Amemiya, and K. Kuwajima, *Protein Sci.* **12**, 672 (2003).
43. R. Stegmann, E. Manakova, M. Röble, and H. Heumann, *J. Structural Bio.* **121**, 30 (1998).

44. M. A. Anisimov, *Critical Phenomena in Liquids and Liquid Crystals* (Gordon and Breach, Philadelphia, 1991).
45. J. V. Sengers, *Int. J. Thermophys.* **6**, 203(1986).
46. A. Kostko, M. A. Anisimov, and J. V. Sengers, *Phys. Rev. E.* **76**, 021804 (2007).
47. A. Kostko, M. A. Anisimov, and J. V. Sengers, *Phys Rev E.* **66**, 020803 (2002).
48. H. Tanaka, Y. Nakanishi, and N. Takubo, *Phys. Rev. E* **65**, 021802 (2002).
49. M. Adam and M. Delsanti, *Macromolecules* **18**, 1760 (1985).
50. T. Jian, D. Vlassopoulos, G. Fytas, T. Pakula, and W. Brown, *Colloid Polymer Science* **274**, 1033 (1996).
51. T. Nicolai, W. Brown, R. Johnsen, and P. Stepanek, *Macromolecules* **23**, 1165 (1990).
52. P. J. Collings, *Liquid Crystals: Nature's Delicate Phase of Matter* (Princeton University Press, Princeton, 1990).
53. P. J. Collings and M. Hird, *Introduction to Liquid Crystals: Chemistry and Physics* (Taylor and Francis, New York, 1997).
54. Y. A. Nastishin, H. Liu, S.V. Shiyankovskii, O. D. Lavrentovich, A. F. Kostko, and M. A. Anisimov, *Physical Review E*, **70**, 051706 (2004).
55. A. F. Kostko, B. H. Cipriano, O. A. Pinchuk, L. Ziserman, M. A. Anisimov, D. Danino, and S. R. Raghavan, *J. Phys. Chem. B* **109**, 19126 (2005).

56. J. Lydon, *Curr. Opin. Colloid Interface Science* **3**, 458 (1998)
57. J. E. Lydon, in *Handbook of Liquid Crystals*, edited by D. Demus, J. Goodby, G. W. Gray, H.-W. Spiess, V. Vill, vol. 2B, Chapter XVIII, *Chromonics* (Wiley-VCH, New York, 1998) p. 981.
58. N. H. Hartshorne and G. D. Woodard, *Mol. Cryst. Liq. Cryst.* **23**, 343 (1973).
59. L. D. Landau and E. M. Lifshitz, *Statistical Physics* (Oxford, New York, Pergamon Press, 1980)
60. P.G. de Gennes, *The Physics of Liquid Crystals*, 2 ed. (Clarendon Press, Oxford, 1993).
61. B. J. Berne and R. Pecora, *Dynamic Light Scattering with Applications to Chemistry, Biology, and Physics* (Wiley, NY, 1976).
62. K. Zero and R. Pecora, in *Dynamic Light Scattering. Applications of Photon Correlation Spectroscopy*, edited by R. Pecora (Plenum Press, NY, 1985).
63. A. Yu. Val'kov, V. P. Romanov, and A. N. Shalaginov, *Physics-Uspekhi* **37**, 139 (1994).
64. M. Doi and S. F. Edwards, *The Theory of Polymer Dynamics* (Clarendon Press, Oxford, 1992).
65. P. S. Russo, in *Dynamic Light Scattering. The Method and Some Applications*, edited by W. Brown (Clarendon Press, Oxford, 1993).

66. M. A. Anisimov in *Dekker Encyclopedia of Nanoscience and Nanotechnology*, ed by J. A. Schwarz, C. Contescu, and K. Putyera (Marcel Dekker, New York, 2004).
67. *Dynamic Light Scattering: The Method and Some Applications*, ed by Wyn Brown (Clarendon Press, Oxford, 1993).
68. K. Shatzel, *Applied Physics B*, **42**, 193 (1987).
69. F. Brochard, and P. G. de Gennes, *Macromolecules*, **10**, 1157 (1977).
70. "All Union Scientific-Research Institute of Physiotechical & Radio Measurements, Moscow" **38**,651 (1980).
71. Kao and B. Chu, *J.Chem.Phys.* **50**, 3986 (1969).
72. B. Chu, *J. Chem. Phys* **41**, 221 (1964).
73. J. W. Tester and M. Modell, *Thermodynamics and Its Applications*, 3rd ed (Prentice Hall, 1997).
74. H. E. Stanley, *Introduction to Phase Transitions and Critical Phenomena* (Oxford University Press, 1971).
75. M. A. Anisimov, A. Kostko, and J. V. Sengers, *Phys. Rev. E* **65**, 051805 (2002).
76. Ian W. Hamley, *Introduction to Soft Matter: Polymers, Colloids, Amphiphiles and Liquid Crystals* (Wiley&Sons, West Sussex, 2000).

77. K. Kawasaki, *Phase Transitions and Critical Phenomena*, ed. C. Domb and M. S. Green, (Academic, New York, 1976).
78. C. Domb and M. S. Green, *Phase Transitions and Critical Phenomena* (Academic, New York, 1976).
79. H. C. Burstyn, J. V. Sengers, J. K. Bhattacharjee, R. A. Ferrell, *Physical Review A* **28**, 1567 (1983).
80. H. Tanaka, *J. Phys. Condens. Matter* **11**, L159 (1999).